University of Amsterdam

Masters Thesis

Optimizing b-value Composition For Maximizing ADC Contrast between Cancerous and Healthy Breast Tissue using a Diffusion Weighted MRI Simulator

---

Author:
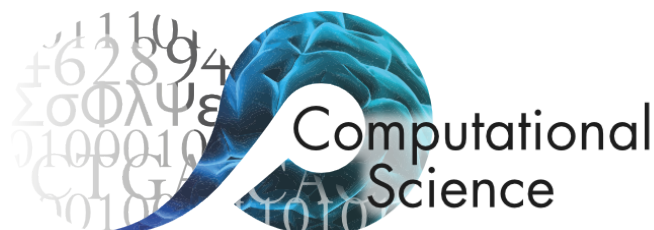
Max Bongers

Supervisors:

Nienke Wassenaar & Natalia Korobova

A thesis submitted in partial fulfilment of the requirements

for the degree of Master of Science in Computational Science

in the

Computational Science Lab

Informatics Institute

June 2023

Declaration of Authorship

I, Max Bongers, declare that this thesis, entitled 'Optimizing b-value Composition For Maximizing ADC Contrast between Cancerous and Healthy Breast Tissue using a Diffusion Weighted MRI Simulator' and the work presented in it are my own. I confirm that:

- This work was done wholly or mainly while in candidature for a research degree at the University of Amsterdam.

- Where any part of this thesis has previously been submitted for a degree or any other qualification at this University or any other institution, this has been clearly stated.

- Where I have consulted the published work of others, this is always clearly attributed.

- Where I have quoted from the work of others, the source is always given. With the exception of such quotations, this thesis is entirely my own work.

- I have acknowledged all main sources of help.

- Where the thesis is based on work done by myself jointly with others, I have made clear exactly what was done by others and what I have contributed myself.

Signed:

Date: July 2023

UNIVERSITY OF AMSTERDAM

Abstract

Faculty of Science

Informatics Institute

Master of Science in Computational Science

Optimizing b-value Composition For Maximizing ADC Contrast between Cancerous and Healthy Breast Tissue using a Diffusion Weighted MRI Simulator

by Max Bongers

In this paper, a Monte Carlo diffusion-weighted MRI simulator is developed to simulate the movement of spins within human breast tissue. The purpose of this study is to determine the optimal b-value and its compositions, for maximizing the ADC contrast between healthy and cancerous breast tissue. Conventional MRI simulations have often oversimplified the signal calculation and microstructural environment. This research adopted a more realistic approach to measuring signal, modeling precession of spins, and the rotation that RF pulses apply to the distribution of spins. Furthermore, the research aimed to create a more realistic representation of the tissue's microstructure. This was achieved by utilizing histopathological data to determine the location and shapes of cell membranes.

The model demonstrated high accuracy for both free diffusion and restricted diffusion, although the accuracy for lower b-values decreased when considering relaxation effects. The results revealed no significant difference between b-values for distinguishing between the tissues types. However some significant differences were found between certain b-value compositions. Compositions with a high gradient strength and a low gradient duration and interval performed worse than compositions with a low gradient strength and a higher gradient duration and interval. This is due the fact that in very short durations, spins do not have time to fully interact with the cell membranes. Consequently, the differences in cellularity cannot be appreciated. Nevertheless, the majority of compositions were not significantly different from each other, likely due to the insufficient level of detail of the microstructure used in the model.

Acknowledgements

This thesis was conducted at the AMC. I would like to express my sincere gratitude to my supervisors Nienke Wassenaar and Natalia Korobova for their continuous advice, interest, feedback and ideas contributed to the research. I'd also like to thank Oliver Gurney-Champion for his contributions to and assistance with the project.

Contents

Chapter 1

Introduction

1.1 What is MRI?

Magnetic Resonance Imaging (MRI), is a medical imaging technique that uses strong magnetic fields, radio waves and magnetic field gradients to create detailed anatomical images. Its uses include disease detection, diagnosis and treatment monitoring. MRI is especially useful in providing information about soft tissues, such as the brain, muscles, and organs, this information includes details about their structure, function, and pathology.

Compared to other imaging techniques such as CT scans, MRI offers better contrast, making it the preferred choice in many clinical scenarios. Additionally, MRI has the advantage of being non-invasive and free from the use of ionizing radiation, which are concerns associated with other imaging methods like X-rays and CT scans. This makes MRI a safe procedure for most people. It is thus no surprise that MRI has become an essential tool in modern medicine, assisting with providing accurate diagnoses and guiding the development of effective and personalized treatment plans for patients [1].

1.2 Purpose of this research

Qualitative MRI scans generates images of anatomical structures without a specific focus on numerical values. Rather than focusing on specific measurements, qualitative MRI relies on signal intensities, which reflect the response of protons to the magnetic fields applied during the imaging process. These signal intensities encode information about the imaged tissues and structures, presenting as varying contrasts on the MRI image. By analyzing these contrasts, abnormalities or lesions can be detected, and important

characteristics such as shape, size, and location can be analyzed [2]. Quantitative MRI on the other hand, can provide quantifiable measurements of tissue properties such as perfusion and diffusion coefficients. This objective information can aid in the early detection of pathological changes and help monitor treatment efficacy, ultimately improving patient outcomes [3]. For instance, a tumor that is well perfused will be more likely to react to chemotherapy than a non-perfused tumor [4]. Additionally, tumors often show diminished diffusion owing to the restriction of movement due to tumor cells [5] [6]. Consequently, treatment can be monitored for efficacy by measuring the rate of diffusion inside the tissue. These examples show how quantitative MRI can be used to develop personalized treatment strategies based on the unique characteristics of a patient's condition, paving the way for a more tailored approach to healthcare. Because of these advantages quantitative MRI holds a lot of potential [3].

Despite its potential, quantitative MRI has some drawbacks, including: longer scan times, increased complexity, poor image quality and measurement errors. To address these issues researchers have been developing advanced acquisition and reconstruction methods, such as compressed sensing and parallel imaging to reduce scan times and improve image quality. Furthermore, the development of standardized protocols and the integration of artificial intelligence algorithms have helped streamline quantitative MRI workflow and enhance diagnostic accuracy. Still, the aforementioned issues persist and are the reason quantitative MRI is not the first choice of many clinicians [3] [7].

As previously mentioned, different tissues exhibit variations in diffusivity which allows them to be distinguished from eachother. This is achieved by measuring the apparent diffusion coefficient (ADC), which quantifies the diffusion of tissues, representing the observed diffusion constant inside tissue. The ADC values are influenced not only by inherent properties of the medium but also by factors such as microstructural barriers and cell membranes that restrict particle movement [8]. Imaging techniques that utilize the ADC to acquire images are known as diffusion-weighted imaging (DWI). DWI possesses the capability to examine tissue structure at the cellular level, making it effective at estimating tissue celularity [9].

The acquisition parameters that are used in DWI can heavily affect the resulting image. Different combinations of parameters can be used to optimize the contrast in specific tissues and pathologies [10]. Finding the best acquisition parameters to find the highest contrast between healthy tissue lesions is thus important. One of the most crucial acquisition parameters is called the 'b-value', which is a parameter that determines how sensitive the imaging is to particle movement in tissues. Adjusting this value allows for capturing information about the microscopic structure of tissue. The b-value itself consists of three parameters: the gradient strength (G), the gradient duration (δ), and

the time between gradients (Δ). These parameters control the sensitizing of the signal to diffusion through gradient magnetic fields [8].

Due to the complex nature and technical challenges involved in DWI, simulations are often used to develop new acquisition parameters and increase understanding on the topic. Simulations of MRI experiments offer several advantages: Firstly, it eliminates the need for a patient to be present in the machine as no actual scan needs to be performed. This reduces costs and can potentially save time if the simulation is efficient. Additionally, the ground truth is often known when running simulations, which makes it easier to investigate and validate the results of different parameters on the quality of the scan.

To simulate MRI scans there are two main approaches: analytical and model-based. Both approaches have their advantages and disadvantages. Analytical approaches use mathematical equations to describe the physics of MRI directly, this offers advantages such as speed and simplicity, allowing for quick computations and straightforward solutions for simplified scenarios. However, it has limitations in handling more complex real-world scenarios, it can lack accuracy due to making assumptions and simplifications and has limited flexibility in accommodating different imaging techniques. A model-based approach has more flexibility, allowing for realistic and customizable simulations that can represent complex scenarios. Furthermore, it has the potential to provide more accurate results by incorporating detailed modeling of cell structures. However, it has a greater computational cost and often requires more validation efforts [11].

There have been many papers that use model-based approaches in the context of MRI. For instance, one study employed Monte Carlo simulations to explore the optimal value of b for estimating white-matter fiber orientations using diffusion MRI with a standard spherical sampling scheme [12]. Other work tries to find the optimal b-value to measure intravoxel incoherent motion parameters using Monte-Carlo simulations [13]. Additional, more general model-based MRI simulations have been done incorporating swelling, abutting, and deformation within complex irregular substrates [14].

In contrast to the research discussed above, which simplifies the microstructural intricacies of human tissue, this study seeks to bridge this gap by integrating real histopathological data on the location and shapes of cells. Employing a model-based approach that uses a Monte Carlo model to simulate particle movement, a more realistic diffusion simulation is created that takes into account the structural complexities that previous research has not. Additionally, in conventional MRI simulation studies the signal calculation is often simplified and does not accurately represent the underlying processes. This research further aims to simulate the workings of the imaging process more closely by adopting a more realistic approach to signal measurement.

Acknowledging the gap in the current literature and the importance of the acquisition parameters in MRI scans, the research question for this paper is: What are the optimal b-values and compositions that maximize the ADC contrast between healthy and cancerous breast tissue, using a diffusion weighted MRI simulator?

The hypothesis for the research question posits that the inclusion of cell locations and shapes, derived from histopathological data, coupled with a more realistic approach to signal measurement, will lead to a more accurate estimation of the optimal b-values and b-value compositions. Although there is limited research employing a model-based approach to find the optimal b-value and its composition for tumor detection, prior empirical studies indicate that the optimal b-value for differentiating breast tumors is approximately equivalent up to a value of 1500 s/mm^2. Although a b-value of 1500 s/mm^2 performed the best, with a slight margin, beyond which the signal contrast decreased [15] [16]. Hence, an approximate b-value of 1500 s/mm^2 is anticipated based on these findings. Given the disparities in cellularity between healthy and cancerous breast tissue, it is further hypothesised that the duration components δ and Δ will play a more significant role in determining contrast than the strength component G. A combination of high strength and long duration might render the tissues indistinguishable, whereas a combination of high strength and a short duration might not adequately sensitize the signal to diffusion in the tissues. Hence, the optimal b-value will likely be one with low strength and a long duration.

1.3 The basics of MRI

An atom is a particle of matter that uniquely characterizes a chemical element. Atoms consist of a nucleus and a shell, inside the nucleus are protons. The protons have angular momentum which means they are continuously spinning around an axis, this spinning motion gives the proton an electric charge. Furthermore, the electric charge itself rotates, generating an electrical current that, in turn, generates a magnetic field. Thus the proton itself can be seen as a little bar magnet. These protons, often referred to as 'spins' form the foundation of what enables the functionality of MRI [8].

Not every element can be used in MRI, one requirement is that the element cannot have an equal number of spins and neutrons in its nucleus. If the nucleus is balanced it will not undergo the magnetic resonance effect necessary for MRI. In practice the element used in image acquisition is almost always hydrogen. This is because of its abundance in the human body and its relatively strong MR response [8].

The MRI scanner uses a strong magnet to generate a magnetic field, which creates a torque or "twisting force" acting perpendicular to both the field and the direction of the angular momentum. The spin is deflected into a circular path perpendicular to the field [8]. The resultant circular motion is called precession. An example is Earth, which is precessing at an angle around its axis. Figure 1.1 shows a spin precessing around the static magnetic field.
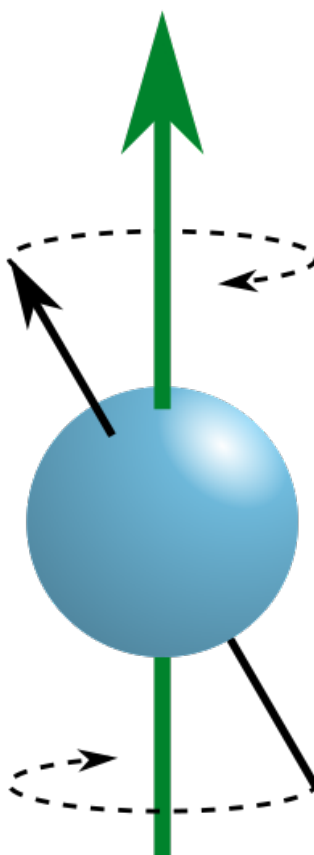

FIGURE 1.1: A precessing particle. The green arrow is the externally applied magnetic field, the black arrow is the angle of precession created by the external magnetic field [17].

In the absence of an externally applied magnetic field all spins are oriented randomly. When the external magnetic field of the MRI scanner is turned on spins will, on average, point more in the direction of this magnetic field. This is called 'alignment', the outcome of this alignment is a slight excess in the direction of the magnetic field, which is ultimately responsible for the signal measured in MRI. Figure 1.2 shows a collection of spins that is aligned with a magnetic field, the alignment is indicated by the large vertical arrow [18].

Because the spins are initially oriented randomly in a 3D environment with orientations along the X, Y, and Z axes, the sum of their individual components cancel each other out. When the magnetic field is turned on, usually considered to be along the 'Z-axis', the
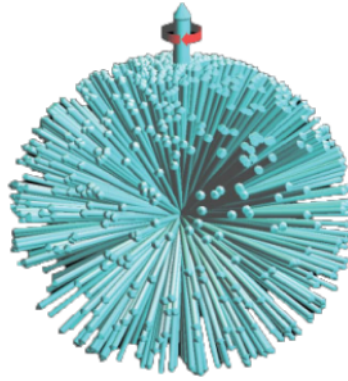
FIGURE 1.2: Representation of spins aligning with the magnetic field [18]. (N.B. the spins are not actually all in the same place, this is done for clarity).

spins will now align themselves along the Z-axis. Because of this alignment there is now a slight excess in the sum of the Z components of the spins while the X and Y components still cancel each other out due to their random orientations. This excess alignment along the Z-axis is called longitudinal magnetisation because it's along/longitudinal to the magnetic field. This magnetisation serves as the foundation for generating the MR image. Figure 1.3 shows a simplified example, the spins are precessing around the Z-axis, the X and Y components completely cancel themselves out, and most of the Z components cancel themselves out. However, a slight excess along the Z-axis remains [8].
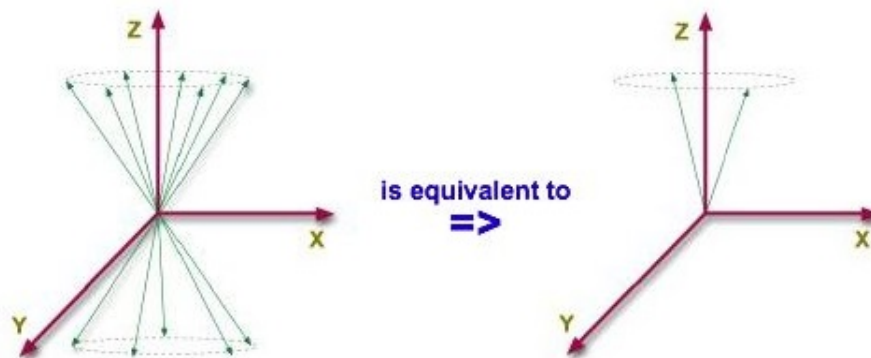
FIGURE 1.3: Longitudinal magnetisation due to alignment with magnetic field. This figure is simplified for clarity, the actually orientation of spins is more akin to figure 1.2 [19].

The longitudinal magnetisation is, as previously discussed, parallel to the applied magnetic field. This magnetisation is vanishingly small compared to the magnetic field, which makes it near undetectable. Aside from the longitudinal magnetisation there is also transverse magnetisation, which is perpendicular to the magnetic field (the X and

Y components in this case). Due to this perpendicularity, if the orientation of the magnetisation is changed into the transverse plane it becomes possible to detect it. This can be done using an RF (radio-frequency) pulse [20].

1.4   The RF pulse

Resonance is a phenomenon that occurs when an object or system absorbs energy from an external stimulus that matches its natural frequency of oscillation. An example is the tuning fork: suppose we have three tuning forks, two of which are tuned to the note 'A,' while the third is tuned to the note 'D.' If we strike one of the A-tuned forks, the other A-tuned fork will begin to produce the same sound. However, the D-tuned fork will not resonate since its natural frequency differs from the frequency of the stimulus, resulting in a lack of energy transfer [21].

As mentioned before the spins are precessing around the static magnetic field. How quickly they precess depends on the strength of the main magnetic field 'B0' which is measured in Tesla (T), and the gyromagnetic ratio of the spin γ, measured in radian per second per Tesla. The gyromagnetic ratio is a property of an atom that describes how it interacts with an external magnetic field. Specifically, it describes the ratio of the magnetic moment of the nucleus to its angular momentum. The gyromagnetic ratio of a nucleus depends on a few factors, including its mass, charge, and spin. The frequency of precession ω is then given by the Larmor frequency: [22]

$$\omega = -\gamma B \tag{1.1}$$

Different elements exhibit distinct precessional frequencies. For example, hydrogen possesses a gyromagnetic ratio of approximately 42 MHz. This means that at a magnetic field strength of 1 Tesla the frequency of precession amounts to 42 MHz. Leveraging this known frequency, resonance can be used to rotate the spin distribution. This is done using an RF pulse: a magnetic field B1 is turned on in a direction perpendicular to B0, then turned off and immediately another magnetic field in the opposite direction is turned on, still perpendicular to B0. This back and forth switching of magnetic fields is done at the Larmor frequency of the spins. As a result, the spins are effectively 'pushed' or 'pulled' by the oscillating field, causing them to rotate away from their equilibrium direction into the transverse plane. The degree of rotation is dependent on the strength and the duration of the RF pulse. A 90-degree pulse will rotate all spins by 90-degrees, in which case all of the longitudinal magnetisation is rotated into the transverse plane. Figure 1.4 shows an RF pulse on a system of spins [23].
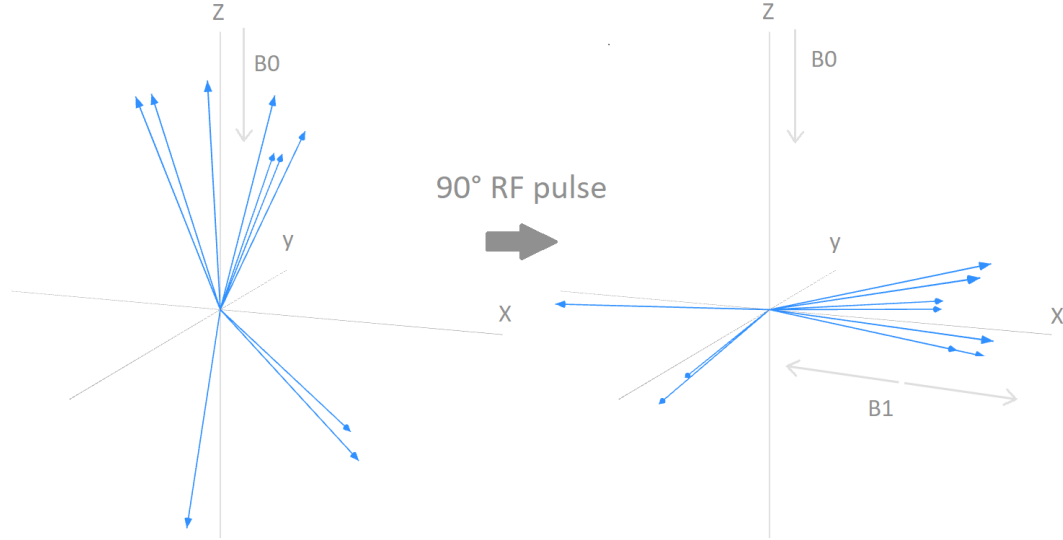
FIGURE 1.4: Rf pulse example. Note that the rotation in this example was done along the Y-axis, this is an arbitrary choice and can be done along the X-axis as well. Both of these operations rotate the longitudinal magnetisation into the transverse plane.

After the RF pulse there is now some measurable signal because the magnetisation is no longer aligned with B0, and B1 is turned off. The cumulative total of all spins residing in the transverse plane is referred to as the transverse magnetisation, while the aggregation of spins in the longitudinal plane is termed the longitudinal magnetisation. The amount of transverse magnetisation is also called 'phase coherence' or as the spins being 'in phase' with each other. After the RF pulse the spins are still precessing around the magnetic field at the Larmor frequency. Because they are precessing at (around) the same frequencies they keep pointing in the same direction, they stay 'in phase' [20].

1.5 Relaxation

When B1 is turned off the transverse magnetisation gradually decays, while the longitudinal magnetisation gradually returns to its original level. This phenomenon is referred to as relaxation. Longitudinal relaxation, also known as 'T1 relaxation', is governed by a time constant called T1. Similarly, transverse relaxation, known as 'T2 relaxation', is determined by a time constant called T2. Generally, T1 is longer than T2. The durations of T1 and T2 depend on various factors, including field strength and tissue type. The T1 relaxation process can be described by the following equation: [24]

$$M_z = M_0(1 - e^{-t/T1}) \tag{1.2}$$

Where t is the time lapsed after the RF pulse and M_0 is the amount of longitudinal magnetisation before the RF pulse. At t = T1, the signal will have recovered 63% of its original value. Figure 1.5 shows the T1 relaxation curve.
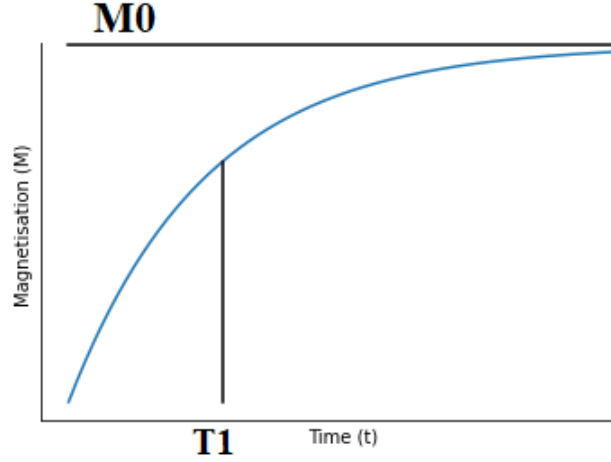
FIGURE 1.5: T1 relaxation curve.

Following the RF pulse, the initial longitudinal component is transformed into the transverse plane. However, the relaxation process is not merely a reversal of this rotation. T1 relaxation and T2 relaxation occur due to distinct mechanisms and at different rates, albeit simultaneously. The main cause for T1 relaxation is spin-lattice interactions: this process involves the transfer of energy that the spins received from the RF pulse to their surrounding molecules, nuclei and atoms. This transfer of energy occurs through collisions, rotations and electromagnetic interactions. T1 relaxation is thus an energy flow between spins and their environment. This process can cause the spins to lose their excess energy and go back to their equilibrium state, which results in T1 relaxation [25].

T2 relaxation is described by the following equation: [24]

$$M_{xy} = M_0 e^{-t/T2} \tag{1.3}$$

At t = T2, the signal will have decayed to 37% of M_0. In figure 1.6 the T2 relaxation curve can be seen. The analytical equations for T1 and T2 relaxation are also called the 'Bloch equations'.

FIGURE 1.6: T2 relaxation curve.
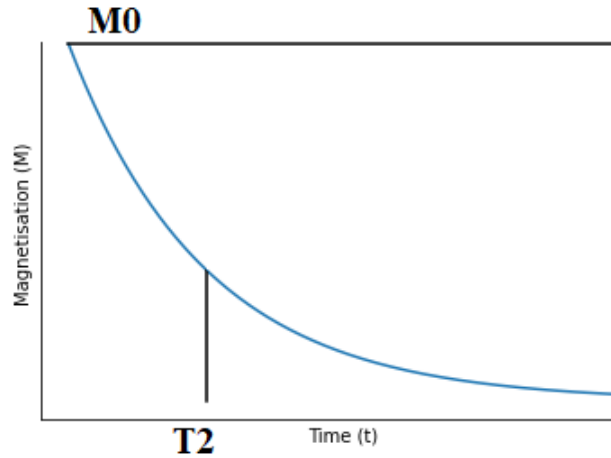
The main causes for T2 relaxation are: [25]

- Spin-spin interactions: spins have a chance to interact with neighboring spins which can result in the transfer of energy between them. This transfer of energy can lead to a change in orientation of the spin. Because there is phase coherence in the transverse plane, changing the orientations of spins will lead to T2 relaxation.

- T2 relaxation because of T1 relaxation: when a spin-lattice interactions occurs involving a spin that is contributing to the transverse magnetisation, its orientation would randomly change, which results in T2 relaxation

In addition to T2 relaxation there is also T2* relaxation, which takes into account inhomogeneities in the magnetic field of B0. The precessional frequency of spins depend on the magnetic field strength, due to hardware imperfections and molecular environmental differences, the magnetic field strength is not uniform across the scanner. This means that spins can precess at different frequencies, which results in them going out of phase and thus results in relaxation. Since T2* incorporates this additional form of relaxation it is always shorter than T2. Signal loss caused by inhomogeneities and molecular differences can be recovered using a 180-degree RF pulse in a spin echo sequence.

1.6 Spin echo sequence

Magnetic field inhomogeneities cause the spins to process at varying frequencies, leading to a faster loss of phase coherence. Consequently, this phenomenon leads to a reduction in signal strength. Assuming spins are stationary, this effect can be reversed using a 180-degree RF pulse. This pulse effectively flips the distribution of spins upside down,

reversing the directions of precession. As a result, the faster precessing spins that were previously 'ahead' of the slower ones are now 'behind' them and will catch up, restoring phase coherence. The highest signal strength is observed after the same duration of time has passed since the 180-degree RF pulse as between the 90-degree RF pulse and the 180-degree pulse. This specific time point is known as the time of echo or 'TE'. Therefore, the 180-degree pulse occurs at the time point TE/2. The spins dephasing and rephasing can be seen in figure 1.7 [26].
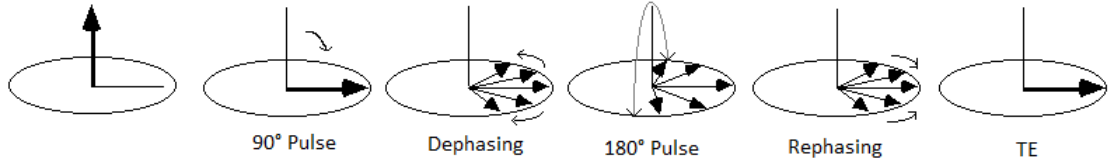
FIGURE 1.7: A system of spins dephasing and rephasing after a 180-degree pulse. Note that in reality the spins are not all pointing in exactly the same direction, there is only a slight excess of the sum of all spins in the transverse plane [27].

1.7 Diffusion weighted imaging

In addition to precessing, spins within the tissue are in constant motion. This motion can be exploited to differentiate between spins that are moving rapidly versus those that are moving slowly. This is achieved by applying an externally generated gradient magnetic field, the strength of which is denoted by 'G'. The gradient linearly increases in strength from -0.5G to 0.5G across the the axes. This gradient is called the motion-encoding gradient which will be, for simplicity's sake, referred to as 'the gradient' for the remained of this paper.

Owing to the dependence of precessional frequency on the Larmor equation, the linear variations in the magnetic field strength induced by the gradient cause the spins to precess at different speeds. This disparity enables the differentiation based on their movement characteristics. Figure 1.8 shows the gradient increasing along the magnetic field.

FIGURE 1.8: Schematic of MRI scanner with gradient coils [28].

In the middle of the magnetic field, also known as the 'isocenter,' the magnetic field strength of the gradient is 0, which causes the spins to precess at the Larmor frequency.
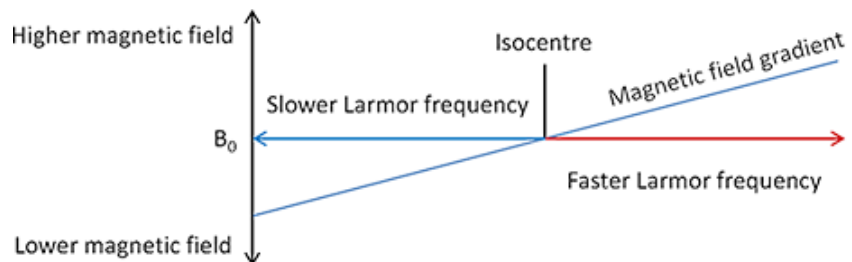
As explained previously, in the spin echo sequence, the 180-degree pulse is used to restore the phase coherence by reversing the spin direction. However, due to the spins' motion and the presence of the gradient field the faster the spins are moving, the more phase is lost. This is because faster-moving spins experience larger variations in field strength compared to slower-moving spins.

Due to the motion, the 180-degree pulse cannot completely restore the spins to perfect phase coherence, owing to the different field strengths experienced by the spins before and after the pulse. This discrepancy in phase can be measured by acquiring an MRI scan without a gradient as a baseline image, and then comparing it to an image acquired with a gradient applied. The strength of the signal difference between these images is determined by the degree of spin movement, or in other words, the level of diffusion in the tissue [29].

As mentioned briefly in the introduction, the b-value is an acquisition parameter that determines how sensitive the imaging is to the movement of spins. The b-value is determined by three parameters: the gradient strength 'G' which represents the amplitude of the magnetic field gradient, the duration of the gradient 'δ' and the time between gradient pulses 'Δ'. Figure 1.9 shows the effect of the different parameters in the imaging process.
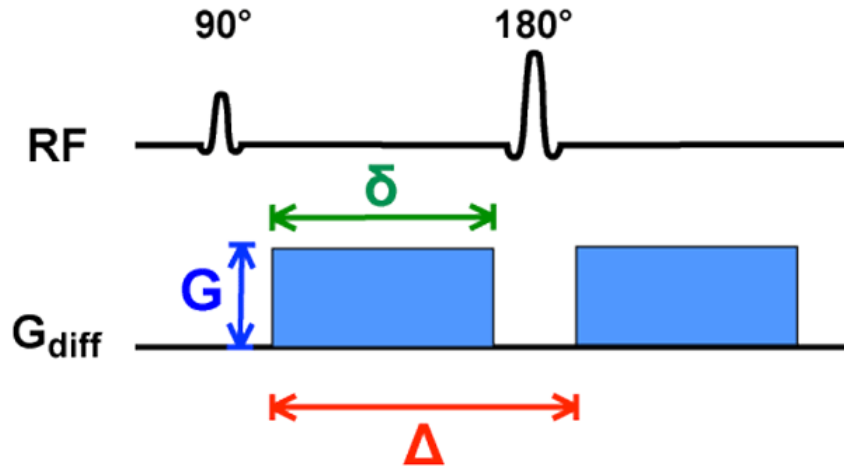
FIGURE 1.9: The effect of the 'G, 'δ' and 'Δ' on a spin echo sequence [30].

Δ is not affected by G directly. However, it provides the spins with more time to diffuse between the application of gradients. As a result, the spins move farther away from their initial positions during the first gradient, leading to a greater loss of phase. As the b-value increases, the imaging becomes more sensitive to diffusion resulting in a greater

loss of signal during the acquisition. The b-value can be calculated using the following equation: [31]

$$b = \gamma^2 G^2 \delta^2 (\Delta - \delta/3) \tag{1.4}$$

The b-value is commonly expressed in units of s/mm^2 because it represents a combination of time and space factors. The time factor corresponds to the duration of the gradients, while the space factor relates to the fact that gradient strength is measured in mT/m. Typical values of b range between 0 and 3000 s/mm^2, varying based on factors such as tissue type and the specific imaging protocol.

Signal attenuation refers to a reduction of the signal's intensity. Signal attenuation due to the gradient can be described by the following equation: [31]

$$S = S_0 e^{-bD} \tag{1.5}$$

Where D is the diffusion coefficient, S is the signal intensity measured at TE with a gradient applied, and S0 represents the signal intensity without a gradient applied. Higher values of b and D result in greater signal attenuation.

Due to the greater signal attenuation, the signal-to-noise ratio (SNR) of high b-values is worse than for lower b-values. The SNR quantifies the intensity of the signal relative to the level of noise present and is inversely proportional to the b-value. Conversely, the contrast-to-noise (CNR) quantifies the relative difference in signal intensity of two regions, relative to the level of noise present [32]. In this research, CNR will quantify the difference between a signal with and without a gradient applied, relative to the noise present.

1.8   Monte Carlo and random walker

The fundamental principle underlying Monte Carlo simulations lies in obtaining a large amount of random samples to obtain a numerical result [33]. In this research, each individual spin can be considered as one sample of the Monte Carlo simulation. Each spins' trajectory captures a particular scenario of the spin's movement within in the tissue. According to the Law of Large Numbers, as the number of samples increases, the average of the observed values converges to the expected value. In the context of this research, this means that by simulating a large number of spins an estimate of the signal can be made [33].

The movement of spins is governed by Brownian motion, which is the random motion of particles suspended in a medium. Brownian motion occurs because of collisions between particles and the molecules of the surrounding medium. These collisions make the particles move randomly [34]. In the context of this research, the particles are spins moving around inside human breast tissue. A mathematical process used to describe Brownian motion is the Wiener process, which is a continuous-time stochastic model. While the Wiener process offers a rigorous mathematical description of Brownian motion, it is challenging to directly simulate due to its continuous nature.

Because of this, a random walker is often used to approximate a Wiener process. A random walker is a mathematical model that describes the motion of a particle in discrete steps. Each step is determined randomly, without knowledge about the particle's current position or previous steps it has taken. In the limit, a random walker approaches a Wiener process. This implies that as the number of steps increases and the step size becomes smaller, a random walker more closely approximates a Wiener process, and consequently, Brownian motion [35]. Figure 1.10 shows a possible path of a 2D random walker.

FIGURE 1.10: Trajectory of a random walker.

Chapter 2

Literature review

This section will summarize and discuss some of the previous work that has been done regarding MRI simulations and b-value optimization, both empirical and theoretical. This will provide context and shed light on the current state of the literature. Additionally, an expansion will be made on how the existing literature is built upon and contributed to by this research.

Previous empirical studies have investigated how to select the optimal b-value for detecting lesions in breast tissue. Partridge et al. talks about the selection of appropriate b-values. They mention that it depends on the specific imaging application, for instance, there is a distinction between breast imaging and neuro-imaging, the optimal b-values diverge due to variations in the intrinsic properties of the tissue. They further mention that in breast imaging lower b-values are preferred since normal breast tissue has a much higher ADC than other tissues. Finally, they emphasize that ADC measurements of invasive tumors, as well as noncancerous breast tissue, depend on the maximum b-value applied [32].

There have also been studies that found no significant difference in the ability to distinguish between breast tissue types for b-values up to 1000 s/mm^2 [36]. Other research found a b-value of 1400 s/mm^2 to be only slightly superior to a value of 700 s/mm^2 [16]. This indicates that although the b-value has an impact on the absolute value of the ADC, previous research has not definitively found the optimal b-value to distinguish between breast tissue types.

Another empirical study into the effect of the gradient strength on axon diameter and density estimations, found that a higher gradient strength increased contrast between different regions in the brain. Furthermore, the known variations in axon diameter and density across different regions of the corpus callosum remained consistent and

became more reproducible at higher gradient strengths [37]. Although this research was performed in the brain, the estimation of axon diameter and density ultimately comes down to the amount of diffusion taking place and is closely related to the ADC. Consequently, it's possible that a high gradient might contribute to a higher contrast between tissues. Another study found that using a longer δ was beneficial for estimating fibre orientations. The researchers attribute this to an increased signal in the transverse plane of the fibre, and to the increased diffusion time giving spins more room to explore the space, and interact with the environment [38].

There has been little previous research into finding the optimal b-value and its composition to distinguish between tissue types using a model-based approach. However, there have been studies that try to find the optimal b-value for other purposes. One such study investigates the optimal b-value for estimating white-matter fiber orientations using diffusion MRI in a Monte Carlo simulation [39]. Analytical equations are used to synthetically generate the signal, finding the optimal b-value to estimate fibre directions in brain tissue to be 700-1000 s/mm^2. Another study performed Monte Carlo simulations to assess the benefit of the optimal b-values in distinguishing malignant from benign lesions [40]. The use of MRI simulations for the optimization of b-values has been relatively limited in existing research. Therefore, part of the contribution of this study lies in its exploration of the potential that simulations have for this purpose.

Jelescu et al. talk about how model-based approaches are inherently a simplified version of reality. They mention that a model can only account for a few, relevant aspects of the tissue it's trying to model. In the context of MRI, the relevant aspects are the microstructural features that affect the signal in a meaningful way. It is thus crucial to choose the correct experimental design when modelling biophysical structures, the model should be designed according to what is being estimated. They give an example of models using parallel cylinders of a given radius, which are often used to model white matter bundles. They mention that for such a model to be valid, and not be biased by other tissue properties not included in the model, the experiment has to have a short diffusion time to make exchange negligible, a very high gradient strength to gain sensitivity to small axons, and a large number of gradient directions to factor out imperfect axon orientation coherence. Only with these conditions would a simple model of cylinders be able to accurately represent the microstructural features of the tissue. Simplifying the model in such a way thus comes with some requirements and limitations on the experiment that is run [11].

Many different numerical and analytical MRI simulation studies have been done that use simplified representations of the microstructural tissue. One study modelled the rate of diffusion in tissue which incorporated swelling, abutting, and deformation. All of

these can affect the amount of diffusion in a tissue, and thus affect the amount of phase coherence of spins. They simulated a 3D environment containing 100 cylinders with radii drawn from a gamma distribution to simulate the cell walls, the swelling of cells is then simulated by increasing the radii. An increase in cell radius due to swelling leads to an increase in tortuosity and a resulting decrease in the ADC. Particles move around with a step size (not drawn from a Gaussian distribution for instance) in a random direction. The movement of spins is impeded by the cell walls, which are not permeable. Each spin is given a 'phase' value, when the spin is moving it will accumulate a 'phase shift', each time step the phase value is changing according to this phase shift. The signal is then measured by summing the phase of each individual spin. Finally the simulation is tested by comparing it to outcomes of analytical models. The researches found that their model agreed with the analytical model for a low amount of overlapping cylinders, and diverged for a higher number of overlapping cylinders [41].

Another study utilised Monte Carlo simulations to estimate inner axon diameter and intra-axonal volume fraction. It assumes a single axon radius rather than one drawn from a distribution, furthermore they assume an equal diffusion coefficient for intra- and extracellular components, but a different diffusivity for longitudinal and transverse directions. For the signal attenuation Van Gelderen's model [42] is used which is an analytical equation that can determine the diameter of a cylinder irrespective of its orientation. Their results show orientationally invariant sensitivity to natural axon diameter distributions [43].

Moreover, Monte Carlo simulations have been employed to investigate the potential of detecting physiological and pathological changes in neurite morphology. When an ischemic event happens in the brain, the changes in ADC in the infarcted region happens quickly, it is known that this change is related to cell swelling, but the precise pathological mechanism is not. They try to model this phenomenon by creating enlargements and constrictions in axons (referred to as 'beading'), this beading substantially decreases the ADC, as happens in infarcted regions. To generate the mesh they created cylinders with different radii, adding beaded regions of the cylinders randomly, the cylinders were packed with a set distance between them. The signal calculation was done the same way as in Hall et al. [41], where individual spins accumulate phase. To validate the model, they used excised rat sciatic nerves, which were subjected to stretching, thereby inducing beading. This hindered the movement of water and significantly decreased the ADC. The results from this experiment were in excellent agreement with the simulated results. They conclude from this that beading accurately captures the restriction of movement due to ischemic events in the brain [44].

There have also been papers that try to take a more realistic way of approaching the mesh creation. In one such paper the following steps are taken to create the mesh: firstly, similar to other research, they generate cylinders with radii drawn from a gamma distribution, and place these parallel to eachother. Secondly, they induce a global orientation dispersion, this is done by randomly selecting one fiber (cylinder) among the population of previously unselected fibers. The selected fiber then has a center of rotation chosen randomly, the fiber is rotated around this point, making sure no collisions with other fibers occur. The third steps of the algorithm involves creating tortuosity in the geometry, this is done by randomly growing or shrinking the radii of the fibers using a Gaussian distribution. The last step of the algorithm involves the inclusion of Ranvier nodes (a gap along an axon) and beading. They then use Monte Carlo simulations to let let the spins diffuse inside the created axons, the signal is calculated using the Gaussian phase approximation, which assumes that the phase distribution of the signal is Gaussian [45]. Their experiments show that the resulting signal was insensitive to the Ranvier nodes added, but very sensitive to beading. The researches conclude by emphasizing the importance of more realistic numerical microstructural representation in order to catch the complexity of the underlying diffusion physics [46].

Another study that tries to create a more realistic mesh investigated the importance of axonal undulation in diffusion MRI measurements. The study employed a Monte Carlo simulation to compare the effects of undulating and straight axons on diffusion. Various parameters, including diffusion propagators, diffusion weighted signal intensities, mean diffusivity and fractional anisotropy were examined. The results showed that the presence of undulation strongly influenced all of these parameters. The diffusivity perpendicular to the undulating axons increased in relation to the undulation amplitude, resembling the diffusivity observed in straight axons with larger diameters. The researchers conclude that when estimating axon diameter using diffusion MR measurements, models assuming straight axons might overestimate the diameter if undulation is present [47].

Additionally, a different study emphasizes the fact that most previous research has used simplified geometrical descriptions of the microenvironments. Neglecting the finer morphological details which could play an important role in the diffusion behaviour. They use Monte-Carlo simulations of particles diffusing in cylindrical compartments, representing neuronal and glial cell fibers as spines and leaflets. Using this representation they investigated to what extent the diffusion weighted signal of particles is sensitive to the neuronal and glial fibers. Their results show that the estimated intracellular tortuosity increases as the spines and leaflets density increases. Suggesting that the finer structures of cell morphology have notable effects on intracellular particles' diffusion behaviour [48].

Another research endeavor tested the validity of a phantom by use of Monte Carlo simulations. Using a similar set-up as in this research, their simulations take place in a square plane of 1 mm by 1 mm, using infinitely extending cylinders. The cylinders' arrangement was differed between being ordered and randomly packed, parallel to eachother, with a set radius. The effects of different geometries were then tested by comparing the estimated diffusion parameters of the different cylinder placements. The parameters obtained through these simulations were in agreement with the observed parameters in the phantom [49].

There have also been studies of two-compartment exchange models of diffusion using Monte Carlo simulations. Once more this research represents axons in white matter as a set of parallel randomly packed non-overlapping identical cylinders with a set radius. They make the assumption that diffusion transverse to the direction of the cylinder is zero. The researches mention this approximation is reasonable because of the long diffusion time compared to the cylinder radius. The signal is then calculated using the coupled Bloch-Torrey equations. The findings of the study were that the Kärger model can be a useful approximation for describing the signal when considering long time intervals, meaning that the residence time in a cell should be much longer than the time it takes to diffuse across it. For greater permeability values the exchange time estimated through fitting to the Kärger model tends to overestimate the actual exchange time, leading to an underestimation of the permeability of the cell membrane [50].

There has also been research that compares analytical outcomes to model-based outcomes. The model-based outcomes were taken from a database of signal curves generated using Monte Carlo simulations, each with different microstructural properties. This was compared to analytical equations based on the two-compartment Kärger model, which calculates signal using the Gaussian phase approximation. They found that the analytical model had a major negative bias, of approximately 25%, in the estimation of intracellular volume fraction. The same bias was not found for the simulation model. As a whole, the simulation model had a higher accuracy compared to the analytical model [51].

Previous research on determining the optimal b-value to differentiate between healthy and cancerous breast tissue has been limited, particularly in the context of a model-based approach. Furthermore, there has been limited research into finding the optimal composition of the b-value for this purpose.

Nevertheless, the studies discussed in this chapter highlight the extensive use of MRI simulations for modeling various phenomena. However, many of these simulations simplify the signal calculation by using analytical equations that make certain assumptions about the phase distribution or the diffusing time. Other papers assign individual spins

phase, and give the spins a phase shift change based on its current time and position. This paper attempts to follow the imaging process more closely by modelling the precession of spins and the rotation that the RF pulses apply to the distribution of spins.

Additionally, as shown in this chapter, previous research has often simplified the microstructural properties of tissue. These simplified models often represent the structure using cylinders, with slight variations across different implementations. Some research tried to more closely model this by incorporating beading and Ranvier nodes, neuronal and glial cell fibers using spines and leaflets, and undulation. This research tries a new approach, using histopathological data to represent the real structure and arrangement of cells, the objective being to more accurately and realistically represent the microstructural properties of human tissue.

Chapter 3

Methods

3.1 MRI simulation

This section will provide explanations and rationalizations for the implementation of certain aspects of the MRI simulation. These explanations aim to shed light on the rationale behind the choices made during the simulation process.

Spins were represented as 3D unit vectors with an X, Y and Z component. The magnetic field was modeled along the Z-axis, which served as the alignment direction for the spins. Every spin was modeled completely parallel to the Z-axis. The initialisation value of the spins was thus a unit vector with a '1' in the Z component. This implementation does not alter the observed results, but it does lead to an increased magnetisation from each spin [18]. The model took the static magnetic field strength in Tesla as an input parameter, and rotated the spins around Z according to the Larmor frequency. The formula for the degree of rotation 'R' of a spin is given by:

$$R = (B0 \, \gamma) \, \delta t \tag{3.1}$$

Where δt is the time step and γ is the gyromagnetic ratio. For the experiments inhomogeneities in the static magnetic field were not taken into account, meaning without an applied gradient all the spins rotated at exactly the same frequency.

3.1.1 90-degree RF pulse

The 90-degree RF pulse was applied by rotating every spin by 90-degrees, meaning all of the longitudinal magnetisation was flipped into the transverse plane. Figure 3.1 shows

the RF pulse being applied to a system, which rotates the system 90-degrees around the Y-axis. This means that all the transverse magnetisation is now concentrated in the X components of the spins. Because the spins were rotating around Z, the transverse magnetisation would rapidly distribute between both the X and Y components.
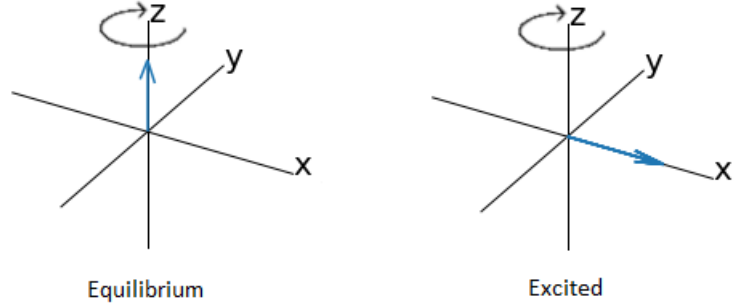

FIGURE 3.1: Phase coherence in the model after a 90-degree RF pulse is applied on an equilibrium state.

To calculate the magnetisation of the system the orientation of all spins was taken into account. In this research, signal is considered to be equivalent to the amount of transverse magnetisation. The formulas used to calculate the net magnetisation are as follows:

$$M_t = \sqrt{(\sum_{i=1}^{n} x_i)^2 + (\sum_{i=1}^{n} y_i)^2}$$

$$M_z = \sqrt{(\sum_{i=1}^{n} z_i)^2}$$

(3.2)

Where n is the number of spins, x_i and y_i are the X and Y components of the ith spin and z_i is the Z component of the ith spin. In words; the norm of the sum of the X and Y components were calculated for the transverse signal, and the norm of the sum of the Z components was calculated for the longitudinal signal. In the figures used in this paper the signal has been normalised between 0 and 1.

3.1.2 Relaxation

Spins do not exist in only one of two orientations, they do not flip between states but transition gradually between the two [18]. To implement relaxation in such a way, the most straightforward implementation of this would involve slowly rotating the spins back to their original state. However, employing this approach did not yield the desired

T1 recovery. This is because, when a vector rotates around the Y-axis, the X and Z components of the vector exhibit non-linear behavior due to the changing projection onto the XY-plane. Even though the rotation itself is steady, the X and Z components undergo sinusoidal oscillations with varying amplitudes throughout the rotation. Consequently, the T1 recovery also becomes sinusoidal rather than exponential.

Thus, a simplified model was implemented, where each spin has two states: spin-up and spin-down. After the 90-degree pulse all spins transition from spin-up to spin-down. T1 relaxation was then modeled by instantly rotating individual spins back by 90-degrees. The probability of this happening was given by the following formula:

$$p_1 = \frac{1}{T1} \tag{3.3}$$

For each time step and spin a random number between 0 and 1 was generated. A comparison was made to check if p_1 was greater than this random number. If the condition was met the spin was rotated back to its original Z position. This process resulted in an exponential recovery of the longitudinal magnetisation. Additionally, this caused T2 relaxation, since a spin rotating back to align with Z makes it lose its XY component.

A similar method as described above was done for T2 relaxation. Spins had a probability of getting a complete random (0-360 degree) rotation around the Z-axis. After this rotation the spin was likely oriented differently than before, and would thus lose phase, meaning T2 relaxation would occur. The probability that this would happen was given by the following formula:

$$p_2 = \frac{1}{T2} \tag{3.4}$$

Again, for each time step and spin a random number was generated, if the number was greater than p_2 the random rotation was applied. This simulated the exponential decay of the transverse magnetisation.

The implementation of relaxation in this research simplifies some of the intricacies of the relaxation process. However, this implementation was justified by the fact that forcing spins into exclusive spin-up or spin-down states, instead of allowing a superposition of both, has no impact on subsequent observations [18]. The implementations were validated by comparing the relaxation curves to the Bloch equations 1.2, 1.3. T1 was varied from 10-1000 ms, T2 was varied from 10-100 ms.

3.1.3 Gradient and 180-degree pulse

The 180-degree pulse was applied by rotating the system 180-degrees around the Y-axis. This operation reversed the direction of rotation of the spins, less importantly it also flipped the sign of the X and Z components. This operation did not influence signal intensity as can be observed in equation 3.2. Figure 3.2 shows what this would look like without a gradient applied.
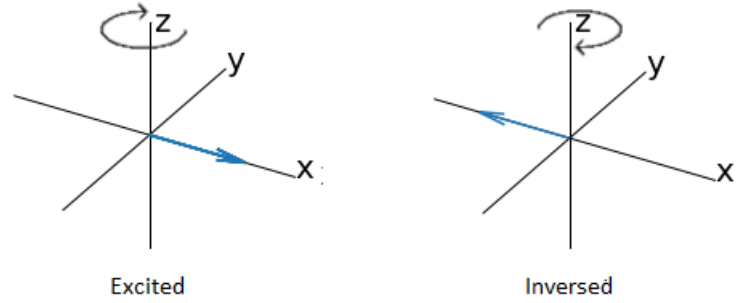

FIGURE 3.2: 180-degree pulse in model.

To implement the gradient, each spin was given a specific location in 3D space, alongside its orientation, with their initial locations uniformly randomized throughout the space. With the gradient active spins precess at varying frequencies, leading to a loss of phase. The formula for the precessional frequency with gradients builds upon formula 3.1.

$$R = ((B0 + (X\,G) + (Y\,G) + (Z\,G))\,\gamma)\,\delta t \tag{3.5}$$

Where R is the degree of rotation that will be applied each time step to each spin, G is the gradient strength and X,Y and Z are the current coordinates of the spin. This simulated the gradient changing the magnetic field strength that the spins are experiencing. The gradient was applied equally in each direction.

3.2 Monte Carlo simulation

This section will delve into the Monte Carlo implementation of the model. As mentioned earlier, spins possess both an orientation and a location in three-dimensional space. In this section only the location of the spins is considered. The spins will undergo random movement throughout the space, which is occupied by cells. The movement of the spins will be modeled via a random walker.

3.2.1 Random Walker

The step size of a random walker can be a set number with a random direction (I.E. -1 or 1), or the direction and magnitude can be drawn from a Gaussian distribution. In this research a set step size was chosen for its slightly higher computational efficiency. The justification for this choice lies in the Central Limit Theorem, which states that when repeatedly summing random values drawn from a distribution the resulting values converge to a Gaussian distribution [52].

The step size l of the random walker was related to the diffusion coefficient in the following way: [41] [53]

$$l = \sqrt{2ND\delta t} \tag{3.6}$$

Where N is the dimensionality of the system, D is the diffusion coefficient and δt is the time step. Each spin took a step of length l in each dimension each time step. The sign of the step, either positive or negative, was randomly chosen with an equal probability of 50%.

For the most accurate result it is advantageous to utilize the smallest possible time step. However, reducing the time step will lead to longer runtime for the model. Assuming free diffusion and no relaxation, the optimal time step was calculated by comparing three different values: 1 ms, 0.1 ms and 0.01 ms. Selecting a smaller time step than 0.01 ms would result in excessively long runtimes. To assess the error of these time steps, the predictions were normalized against the analytical results obtained from equation 1.5. Consequently, smaller b-values were considered equally significant for the error calculation as larger b-values. The error was then compared across the different time steps for varying b-values, and compared to the runtime. The formula used for this was the Root Mean Squared Relative Error: [54]

$$E = \sqrt{\frac{1}{n}\sum_{i=1}^{n}\left(\frac{|estimation_i - analytical_i|}{analytical_i}\right)^2} \tag{3.7}$$

Where E is the error and n is the number of b-values. The closer $\frac{|estimation_i - analytical_i|}{analytical_i}$ is to 1 the better the estimate.

A similar approach was utilized to determine the optimal number of spins in the system. Naturally, a larger number of spins is desirable for improved accuracy, however it is crucial to find a balance between the number of spins and the runtime of the model.

With a time step of 0.1, spin values ranging from 1.000 - 200.000 were tested with a b-value of 1000 s/mm^2. The error was calculated based on equation 3.7 and was compared to the corresponding runtime. Using these methods the time step was set to 0.1 and the number of spins was set to 50.000.

The diffusion coefficient of free water molecules at 37°C is 3×10^{-3}mm^{2}s^{-1} [55]. However, the actual diffusion coefficient of breast tissue is considerably lower [56]. Despite this difference the diffusion coefficient of the model was set at 3×10^{-3}mm^{2}s^{-1}. When the diffusion coefficient is set to match that of free diffusion, spins experience the maximum amount of potential movement expected in an unconstrained environment. Using this, the impact of cell membranes on the ADC could be properly quantified.

3.2.2 Domain and collision detection

The tissue model represents a voxel with dimensions of 1x1x1 mm, establishing the spatial domain in which the spins can move. The simulation domain was designed to be periodic. Ensuring that if spins diffuse beyond the borders of the defined domain, collision detection is performed as if they emerged on the opposite side, mimicking the presence of an identical environment adjacent to it. To achieve this, the spin position was calculated modulo the domain size. It is important to note that this adjustment was only for collision purposes, it was not applied to the spins' actual position, as doing so would introduce significant errors in the gradient calculation.

Although the spins moved in a 3D environment, the cell membranes were only defined in the X and Y planes, meaning there was no obstruction to movement in the Z direction. The cell membranes were approximated with convex and non-convex simple polygons composed of many small walls. Figure 3.3 shows the shapes a cell could and couldn't take.
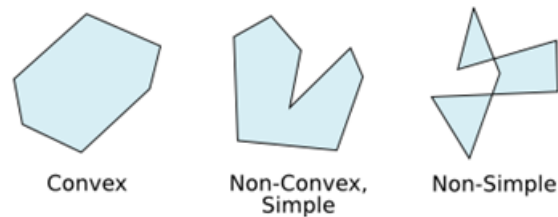

FIGURE 3.3: Clear view of possible and impossible cell shapes.

Because all cells consisted of lines, collision and specular reflection were relatively easy to calculate. Figure 3.4 shows how collision reflects the spin and can reduce the effective step size
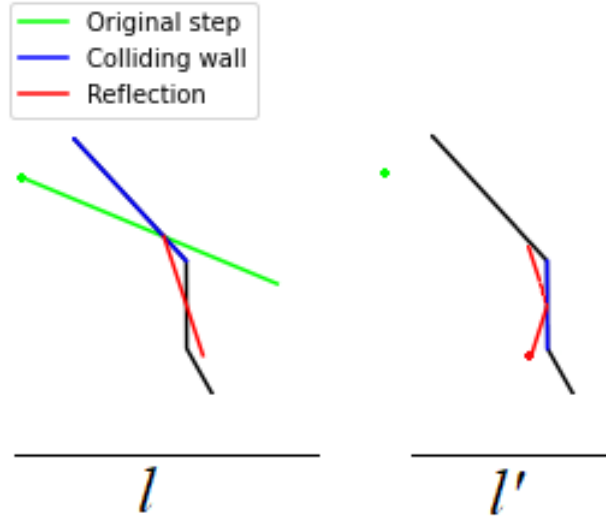
FIGURE 3.4: Reflection for a single step, after the first reflection, there is another collision so the step is reflected again. Step size l is bigger than the reflected step size l'.

The permeability of cells determines the ease with which substances can pass through their membranes. Cell membranes were semi-permeable, the probability p_c of penetrating through them was given by the following formula: [57]

$$p_c = \kappa \sqrt{\frac{6\delta t}{D}} \tag{3.8}$$

Where κ is the cell membrane permeability. To check whether or not a spin should reflect off the cell membrane, a random number between 0 and 1 was generated. If it was larger than p_c the spin was reflected, otherwise it would penetrate the membrane. Previous research used values of 0.01-0.05 mm/s for κ [57] [58] [53]. In this research a value of 0.05 mm/s was used.

The step that a spin takes was determined by the following process:

- Generate a step of size l with a random sign in each dimension

- Check whether or not the spin should go through the cell membrane using equation 3.8. If so, take the step as normal, if not, check if there are any collisions with cell walls

- If no collision occurs, proceed with the step as usual. If a collision is detected, specularly reflect the step and check for collision again. Repeat this process until no more collisions occur, as shown in figure 3.4.

Due to the large number of cells (approx. 10,000) and walls (approx. 130,000) present in the tissue, performing collision checks for each wall at every time step for every spin was computationally infeasible. To address this issue, several optimizations were implemented to enhance the speed of the collision detection algorithm.

- The domain was divided into 625 compartments arranged in a 25x25 grid, overlaying the cells. Each compartment maintained a list of cell walls that exist within it. Some walls may overlap with two compartments simultaneously, resulting in their inclusion in both compartments' lists. The initial step of the collision algorithm involved identifying both the current compartment occupied by the spin and the three closest compartments. The inclusion of the closest compartments is necessary because a spin may be situated close to a compartment border or even multiple compartment borders, and a step could potentially move the spin into another compartment. The walls residing within these four closest compartments were subsequently utilized in the collision detection process. Figure 3.5 shows a visual representation of the closest compartments for a spin.
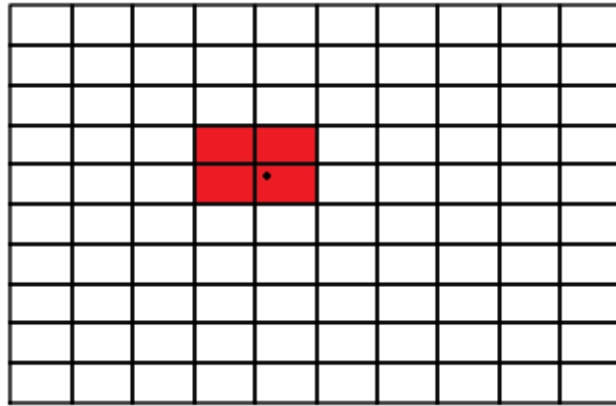

FIGURE 3.5: 10x10 grid of compartments. The spin is marked by the black dot, compartments that will be considered for collision detection are colored in red.

- On average there were only about 1000 walls in 4 compartments, because of this the distance of the spin to each wall could be calculated quickly. This was done by calculating the distance to the midpoint of each wall. The midpoint represents the point that lies equidistant between the two defining points of each wall. This approach was preferred as calculating the distance to a point is faster than the distance to a line. Using these distances, walls that were further away than 0.01 mm were excluded from consideration in the collision detection process.

- The procedure of finding the closest compartments and walls took place once every 5 time steps. Each 5th time step a snapshot of the spin's current local neighborhood was captured and stored for future reference, replacing the old snapshot.

With a step length of l and a time step of 0.1 ms, it was not possible for a spin to move beyond the boundaries of its local neighborhood in 5 steps.

The final collision detection was done by checking for intersections between the line segment connecting the original position of the spin to its updated position after taking a step, and all the walls in its local neighbourhood. In figure 3.6 the local neighbourhood of a spin is shown.
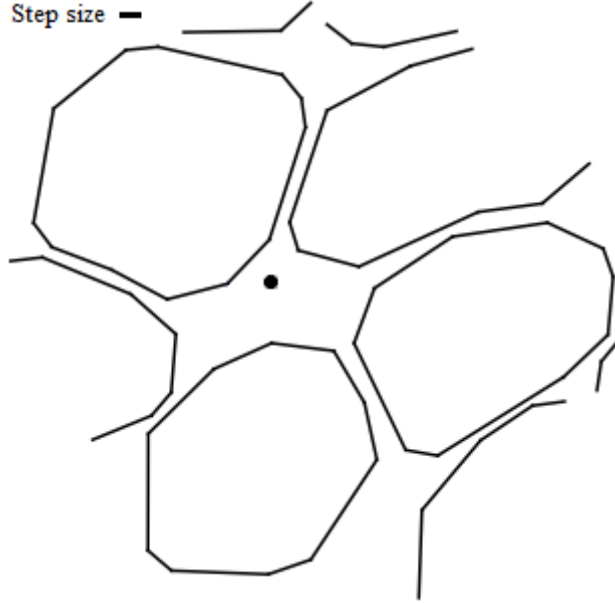

FIGURE 3.6: Local neighbourhood of a spin.

As can be seen in the figure the local neighbourhood contains the cells around the spin. With a step size l, it will not be able to get out of the neighbourhood in 5 steps.

3.3 Histopathological dataset

This section provides an overview of how the histopathological data was obtained and utilized, the process of cell annotation, and the conversion of annotations to XY-coordinates.

The cell locations and sizes were taken from histopathological data of both healthy and cancerous breast tissue. The dataset that was used for this is the BACH (Breast Cancer Histopathological Image Classification) dataset [59]. The BACH dataset is a publicly available dataset that consists of digitized histopathological images of breast cancer tissue samples, along with corresponding annotations. Each image has ground truth labels with up to four classes: normal, benign, in situ, and invasive. The images that were used were 2 dimensional, consequently, the cell data taken from this image was in the X and Y plane. This cell data was then extended infinitely into the Z-plane.

Figure 3.7 shows an example of an H&E stained whole-slide image of the BACH dataset with different cancerous areas labelled.
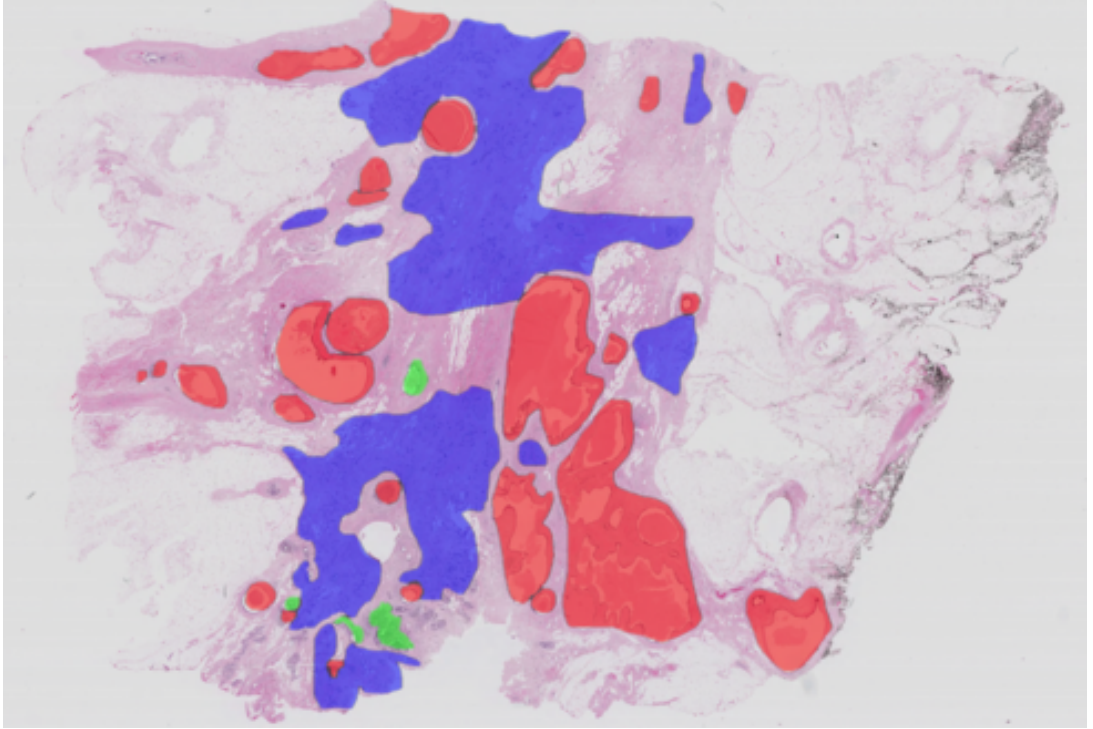
FIGURE 3.7: H&E stained whole-slide image of 6x4cm breast tissue. Different types of cancer are colored. Red: benign, blue: invasive, green: in situ.

In order to examine the signal contrast between cancerous and non-cancerous tissue, cell location data was obtained from normal tissue samples as well as tissue samples labeled as invasive. The primary distinguishing factor between these two categories lying in their cellularity. Figure 3.8 shows an example of these two tissues up close.

FIGURE 3.8: H&E stained tissue. On the left, cancerous tissue, on the right, healthy tissue.

Extracting the cell locations from the histopathological data was done via QuPath, an open-source digital pathology software designed for the analysis, visualization, and annotation of histopathological images [60]. Within Qupath the StarDist plugin was used to detect the cells' nuclei. StarDist is a deep learning-based method that predict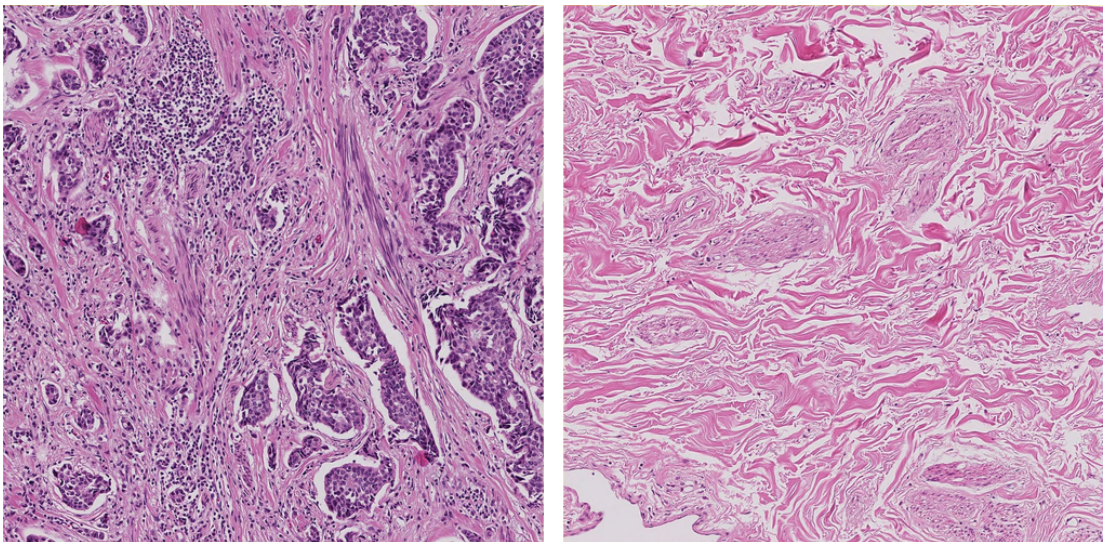s a set of shapes that enclose each nucleus. These shapes, called star-convex polygons, adapt to the individual shape of each nucleus. StarDist comes with a model that is pre-trained on H&E stained images, this model was used in this research [61].

After the nuclei had been annotated, the cell membranes coordinates were acquired by expanding an area around the nuclei to approximate the full cell area. Previous research has used cylinders, with radii ranging from 1-20 µm [41] [62]. In this research, the expanding area was set at 5 µm, theoretically ensuring that the cell membrane was approximately 5 µm away from the nucleus in each direction. In practice, this was usually not the case, the nuclei were often close together and would not have the space to expand that far. When this happened the cell areas of the overlapping cells would be reduced until they didn't overlap.

To calculate the average cell size used in the model the radii of the polygons was approximated by calculating the area of each polygon, then approximating the radius a circle with that same area would have. Using this method the average cell radii for cancerous tissue was calculated at 4.3 µm, and normal tissue at 4.9 µm. Figure 3.9 shows the annotation of nuclei and the cell membranes around it.

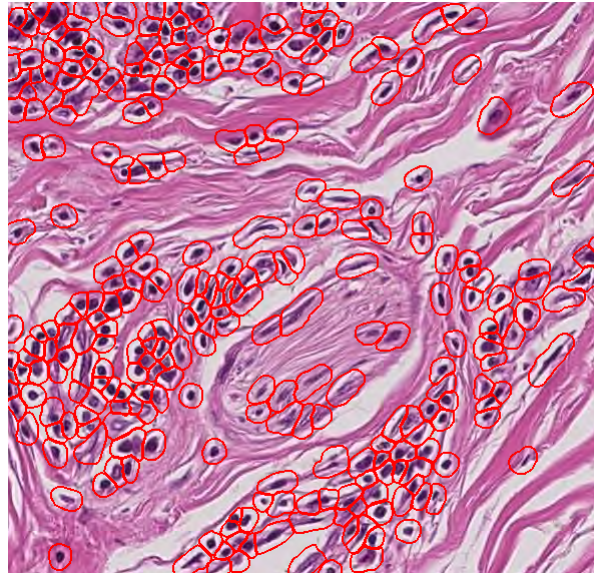

FIGURE 3.9: 250x250 µm image with cell membranes annotated in red.

The annotations are made out of many small walls which are converted into X and Y coordinates and used for collision detection. Figure 3.10 shows the cells of figure 3.8, converted to polygons on an XY-axis.
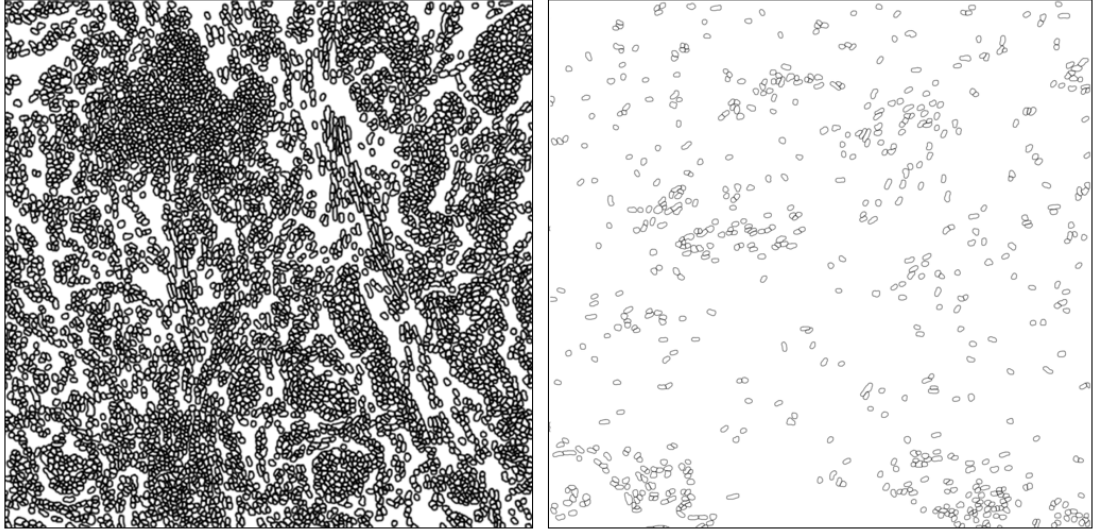
FIGURE 3.10: Polygons of figure 3.8, used for collision detection in the model. On the left, cancerous tissue, on the right normal tissue.

3.4 Validation of model

The validation of a model is a crucial step in assessing its performance and reliability. This section will present a comprehensive overview of the validation methods employed and choices made to evaluate the effectiveness and robustness of the model. All validation simulations were run with a time step of 0.1 ms and 50.000 spins.

3.4.1 Free diffusion

In the case of free diffusion, where there are no cell membranes to restrict movement, the difference in signal between an acquisition with a gradient and without a gradient can be expressed by equation 1.5. To properly validate the model it is important to note that the diffusion coefficient that is used has an impact on accuracy. A higher diffusion coefficient leads to more signal attenuation and a lower SNR, making it more challenging for the model to estimate high b-values. Conversely, a lower diffusion coefficient allows the model to estimate higher b-values more accurately, but it also increases sensitivity to noise at low b-values due to a worse CNR. Validating the model with the free diffusion coefficient of $3 \times 10^{-3} \text{mm}^2\text{s}^{-1}$, without restrictions to movement, would not give an accurate view of the validity of the model. The ADC in normal breast tissue is around $1.5 \times 10^{-3} \text{mm}^2\text{s}^{-1}$ [56] and $0.8 - 1.3 \times 10^{-3} \text{mm}^2\text{s}^{-1}$ [63] in cancerous tissue. Thus the validations were done using a diffusion coefficient of $1.5 \times 10^{-3} \text{mm}^2\text{s}^{-1}$.

To assess the accuracy of the model with as little noise as possible, the simulations were initially run without relaxation, covering a range of b-values from 0 to 6000 s/mm^2 with

various compositions. The same b-values were then tested again, this time incorporating relaxation effects. The relaxation values chosen were representative of normal breast tissue, as those values tend to be lower than those of cancerous tissue (and will thus affect signal estimation more). At 1.5 T, in normal breast tissue T1 relaxation is typically around 1150 ms and T2 relaxation is approximately 57 ms [64]. By utilizing these validation results the limitations of the model could be observed, such as identifying the b-values where the accuracy declined.

The highest and lowest b-value that the model was able to estimate was important to (roughly) find, so the search parameters for the best b-value composition could be bounded. By utilizing the previous validation method it was determined that the highest b-value with accurate estimation was approximately 2500 s/mm^2, while the lowest b-value was around 20 s/mm^2. These estimates were obtained using a diffusion coefficient of 1.5×10^{-3}mm^{2}s^{-1}, it was uncertain whether this would be the actual estimated ADC by the model. Fortunately, it was not very important that these bounds were exact, as the primary goal was to conserve computation time. Based on the findings, the search range was constrained to b-values above 14 and below 3500 s/mm^2.

Rather than the more conventional ADC, the b-values were estimated in the free diffusion validation figures. The motivation behind this decision was to improve clarity. The primary objective of the plot was to offer a clear view of the validity of the changing parameter, which in this case was the b-value. Note that estimating either the b-value or the diffusion coefficient is essentially equivalent, one is substituted for the other using equation 1.5.

3.4.2 Restricted diffusion

Calculating signal attenuation analytically for restricted diffusion poses greater difficulty compared to free diffusion. To address this challenge, a simplified geometry, for which analytical forms exist, was employed to assess the signal attenuation when spin movement is restricted. The shape used for this was a cylinder, extending infinitely in the Z direction. The analytical form was calculated using the the Gaussian phase approximation, which is a method that calculates the signal when spins are restricted by impermeable walls in simple geometric shapes during a spin echo sequence. This is done by calculating the accumulation of phase shifts. The distribution of these phase shifts is Gaussian when the time between pulses is significantly shorter or longer than the time it takes for a spin to diffuse between boundaries. An assumption is made that even when this is not the case, the distribution is still Gaussian. This assumption holds

for simple geometries. The signal is then determined by calculating the mean squared phase change [45].

The analytical form was calculated using Dmipy (Diffusion Microstructure Imaging in Python), which is an open-source toolbox which implements PGSE-based multi-compartment modeling [65]. In these simulations relaxation was not taken into account. The effect of restricted diffusion was tested in three ways: changing the b-values from 0-3000 s/mm^2 by varying gradient strength, changing the cylinder radius from 0.001-0.005 µm, and changing the diffusion coefficient from 0.5 to 3.5×10^{-3}mm^{2}s^{-1}. For each of these the analytical outcome was compared to the model estimation.

Additionally the accuracy of the model was tested for very long values of Δ, where spins are confined within a geometry with impermeable walls. After a certain amount of time the spin will have explored the entire geometry, leading to no further signal loss due to increasing Δ. However, increasing the G parameter should not have the same effect. Thus, simulations were run inside a circle with impermeable walls, where the effect of a long Δ and a high G were tested against eachother.

For these restricted diffusion figures the signal attenuation was estimated instead of the b-values. This was done for clarity as the b-value is not the only parameter being modified. To reiterate, estimating the signal attenuation is equivalent to estimating either D or b.

3.5 Experimental setup for finding optimal b-value and compositions

This section will give an overview of the experimental setup, how the results were obtained and interpreted, which statistical tests were performed, and finally, a summary of all the relevant parameters is provided.

The objective of the experiment was to determine the optimal b-value and its composition in order to achieve the highest ADC contrast between cancerous breast tissue and normal breast tissue. To accomplish this, it was necessary to establish bounds for the range of G, δ and Δ. Gradient strengths typically range from 10-100 mT/m, although there exist gradient coils that go up to 200 mT/m [66]. Thus G was bounded from 10-200 mT/m. Common values for gradient duration range from 10 ms to 40 ms, because short gradient durations add little runtime, δ was bounded between 1 and 40 ms [67] [68] [69]. Values for Δ range from 0-80 ms [70], which is why Δ was bounded at 0-80 ms. Table 3.1 shows the possible discrete values each parameter could take.

N.B. Conventionally Δ includes the duration of δ. However, since the Δ values given in tables 3.1, 3.2 and 3.3 are not directly connected to δ, the Δ values displayed are **only** the time between the gradient blocks, unlike shown in figure 1.9.

δ (ms)	1	5	7.5	10	20	30	40	X	X
Δ (ms)	0	1	5	7.5	10	20	30	40	80
G (mT/m)	10	20	35	50	75	100	150	200	X

TABLE 3.1: All possible discrete values for G, δ and Δ.

Using these specified bounds a grid search was conducted, systematically exploring all possible combinations of table 3.1, resulting in a total of 288 combinations. However, any compositions that generated a b-value exceeding 3500 or below 14 s/mm^2 were discarded. This filtering process resulted in a final set of 142 compositions.

For each composition two simulations were conducted: one on cancerous tissue and another on normal tissue. The ADC values obtained from normal tissue were then subtracted from the ADC values of cancerous tissue to assess their contrast. This process was repeated 15 times for each composition to ensure more reliable results and account for inherent noise in the simulation.

The T1 and T2 relaxations of the two tissue types are not the same: in normal breast tissue T1 relaxation is approximately 1150 ms and T2 relaxation is around 57 ms [64], in cancerous tissue T1 relaxation is approximately 1611 ms and T2 relaxation averages around 83 ms [71] [72]. Table 3.2 shows an overview of all the relevant parameters that were used in the simulations.

Parameter	Value	Meaning
G	10-200 mT/m	Gradient strength
δ	1-40 ms	Gradient duration
Δ	0-80 ms	Gradient interval
D	$3 \times 10^{-3} \text{mm}^2\text{s}^{-1}$	Diffusion coefficient
R	0.004-0.005 mm	Average cell diameter
l	set value based on D	Step size
κ	0.05 mm/s	Cell membrane permeability
N	50.000	Number of spins
δt	0.1 ms	Time step
$T1_n$	1150 ms	T1 of normal tissue
$T2_n$	57 ms	T2 of normal tissue
$T1_c$	1611 ms	T1 of cancerous tissue
$T2_c$	83 ms	T2 of cancerous tissue

TABLE 3.2: Parameters used in the simulations.

The result of the experiment were 142 compositions with 15 data points each. Firstly, the influence of the b-value on the estimation of the ADC was investigated. Subsequently,

the average ADC contrast values for the compositions were calculated and plotted to analyze the overall distribution of contrast values across different b-values. From this three groups could be distinguished: low b-values with high variance, medium b-values with low variance, and high b-values with poor performance overall.

The compositions in the high b-value groups were evidently significantly different from the other two groups, as a result they were excluded from further statistical testing. The group of low b-values had a high degree of variance in its compositions, for instance, some compositions displayed negative contrast values in their samples, which would only be possible if the diffusion inside the normal tissue was lower than that inside the cancerous tissue. In other cases, samples from these same compositions displayed very high contrast. This meant that the contrast values of these compositions were certainly due to noise and not representative of the data. Consequently, any conclusions drawn from these compositions would be dubious. For these reasons only the b-value compositions between 50 and 1500 s/mm^2 were considered for significance tests. After performing this operation, the data now comprised of 92 compositions.

The individual compositions consisted of 15 data points each. To assess if there were significant differences between any two compositions a Kruskal-Wallis test was considered, since the requirement of homoscedasticity for one-way ANOVA was not met [73]. However, due to the large number of groups, the experiment-wise error rate exceeded 99%, resulting in a high likelihood of multiple false positives [74]. Employing post-hoc tests to explore differences between the groups while controlling the experiment-wise error rate, would be too time consuming given the limited time for this research. Moreover, conducting multiple two-group comparison tests would also not be feasible due to the considerable number of groups.

Thus, the different compositions were binned based on their values. Each parameter; G, δ and Δ was sorted in a 'low', 'medium' or 'high' category. The compositions were then divided into bins based on these categories, an example of such a bin is 'low G, medium δ and medium Δ'. A bin with 6 different compositions would then contain 90 samples. With this way of binning there are 3^3 possible bins. Table 3.3 shows the cut off values for different bins.

Bins	**Low**			**Medium**				**High**		
G (mT/m)	10	20	35	50	75	X	X	100	150	200
δ **(ms)**	1	5	7.5	10	20	30	X	40	X	X
Δ **(ms)**	0	1	5	7.5	10	20	30	40	80	X

TABLE 3.3: Binned discrete values for G, δ and Δ.

Not every bin had compositions, for instance bins with high or low in every parameter (because the b-values that would have been in those bins were discarded for being

too high or low). Additionally, bins with only 1 composition were disregarded. After performing these operations a total of 15 bins remained. It should be stressed that the original exact b-value compositions were no longer considered in the data analysis; only the bins in which they were categorized were taken into account. Consequently, each sample within a bin was treated equally in the analysis.

The three bins with the highest average contrast were compared for their significance against all other bins using a Mann-Whitney U test, a non-parametric test which tests the null hypothesis that the distribution of two samples are the same [75]. The reason this test was chosen over a T-test is due to the fact that most of the bins did not have homogeneity of variance.

Because there were 15 bins, each test would be done 14 times for each of the three bins. It was likely that with a p-value of 0.05 there would be false positives, meaning the null hypothesis would be rejected due to random chance. The experiment-wise error for each of the three bins would be $1 - 0.95^{14} = 0.512$ [74]. To correct for this, a Benjamini-Hochberg procedure was done which adjusts the p-values to account for the multiple hypothesis testing [76].

The code and data for the simulation and statistical tests can be found at [1].

---

[1]https://github.com/11349875/MRI-Model

Chapter 4

Results

4.1 Validation of model

This section presents the results of various validation methods employed to assess the performance of the model. The outcomes obtained from these validation approaches will be briefly discussed.

4.1.1 relaxation

Figure 4.1 shows the resulting T1 recovery, together with the analytical form.
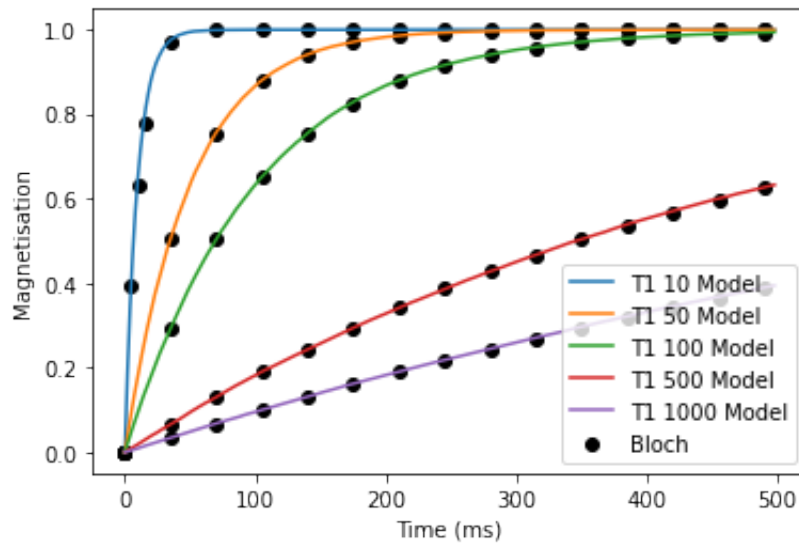

FIGURE 4.1: Longitudinal magnetisation recovery for different values of T1 with 50.000 spins.

Figure 4.2 shows the resulting T2 recovery, together with the analytical form.
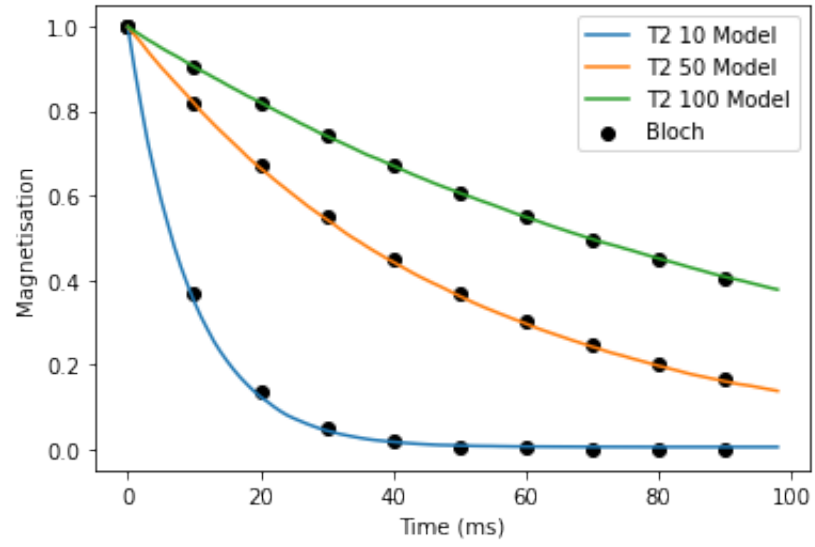
FIGURE 4.2: Transversal magnetisation decay for different values of T2 with 50.000 spins.

As can be seen in figures 4.1, 4.2 the relaxation process closely follows the analytical form for any value of T1 and T2.

4.1.2 Free diffusion

Figure 4.3 presents the estimation of the entire range of b-values without taking into account relaxation processes. To provide a clearer perspective on the estimates for lower b-values figure 4.4 focuses specifically on these lower values.

FIGURE 4.3: Free diffusion with no relaxation, estimation of b-values, D = 1.5×10^{-3}mm^{2}s^{-1}, 50.000 spins. The line indicates where the values would be if the estimated value was equal to the analytical value.
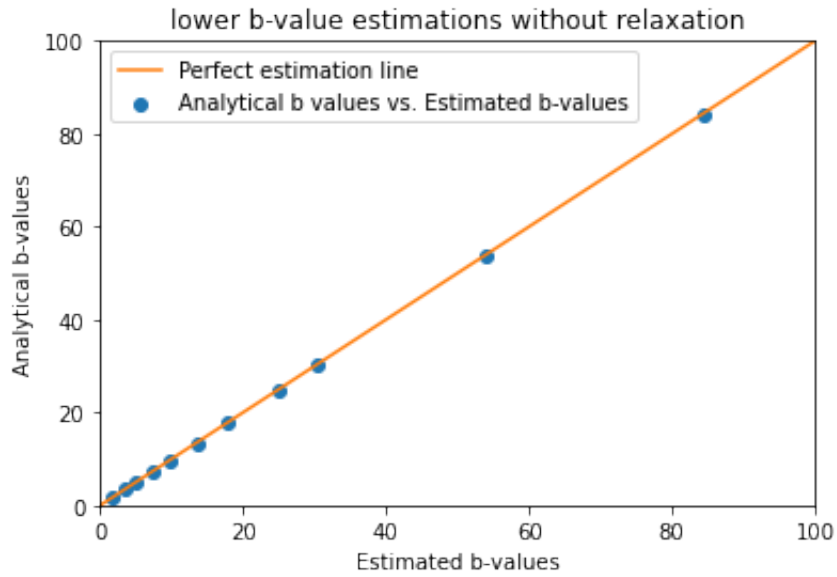
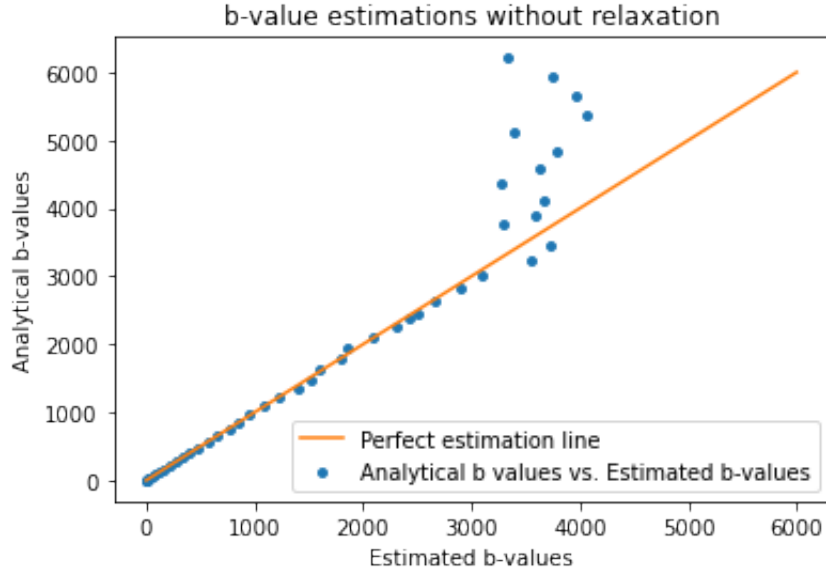FIGURE 4.4: Free diffusion with no relaxation, estimation of lower b-values, D = 1.5×10^{-3}mm^{2}s^{-1}, 50.000 spins. The line indicates where the values would be if the estimated value was equal to the analytical value.

The estimations exhibit remarkable accuracy for b-values below 2000 s/mm^2. Beyond this threshold there is slight deviation from the analytical form, however the estimations

clearly follow the right trend. At a b-value of approximately 3200 s/mm^2, the model is unable to evaluate the signal attenuation correctly. When relaxation is introduced into the system, the accuracy of the model decreases. This is shown in figures 4.5 and 4.6.
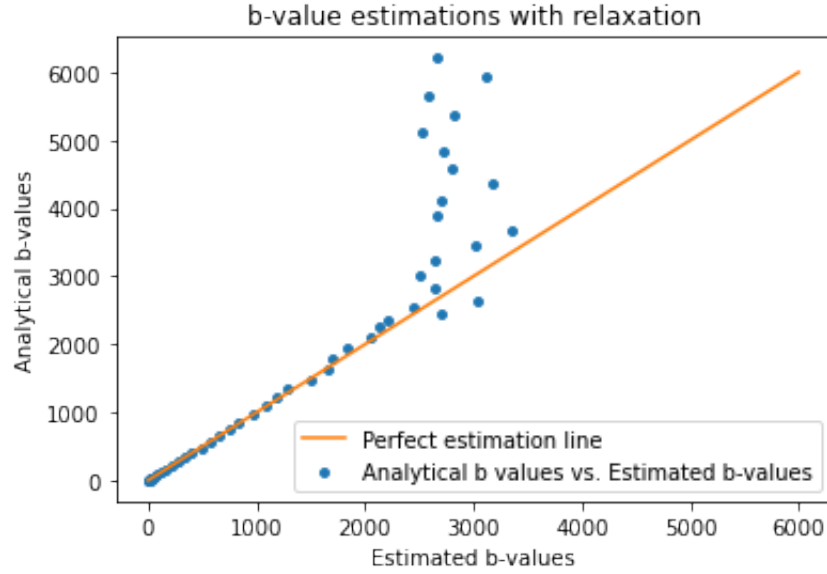
FIGURE 4.5: Free diffusion, T1 = 1150, T2 = 57, estimation of b-values, D = 1.5×10^{-3}mm^{2}s^{-1}, 50.000 spins. The line indicates where the values would be if the estimated value was equal to the analytical value.
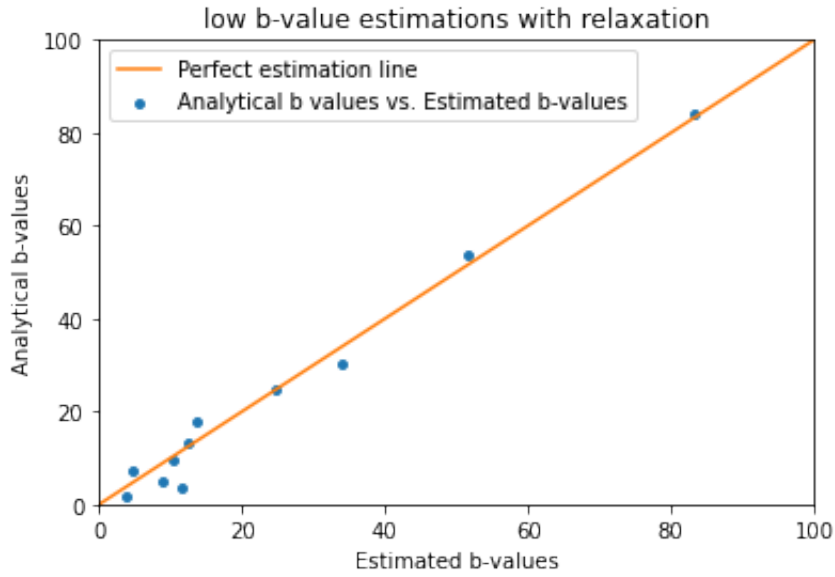
FIGURE 4.6: Free diffusion, T1 = 1150, T2 = 57, estimation of lower b-values, D = 1.5×10^{-3}mm^{2}s^{-1}, 50.000 spins. The line indicates where the values would be if the estimated value was equal to the analytical value.

The highest value of b which the model can accurately estimate is lower, due to the relaxation processes, now being approximately 2500 s/mm^2. The figure also shows a notable deviation from the analytical form for low values of b.

4.1.3 Restricted diffusion

The effect of cylinder radii, b-values and diffusion coefficients on the signal attenuation can be seen in figures 4.7, 4.8 and 4.9.
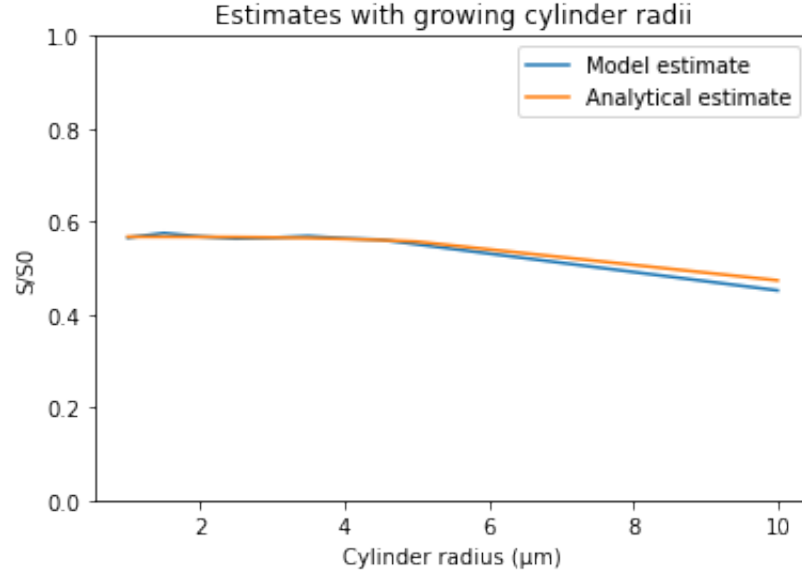
FIGURE 4.7: Model signal vs analytical signal inside cylinder with impermeable wall for different cylinder radii. $D = 1.5 \times 10^{-3} \text{mm}^2\text{s}^{-1}$, 50.000 spins, no relaxation, b-value $= 1000 \text{ s/mm}^2$.
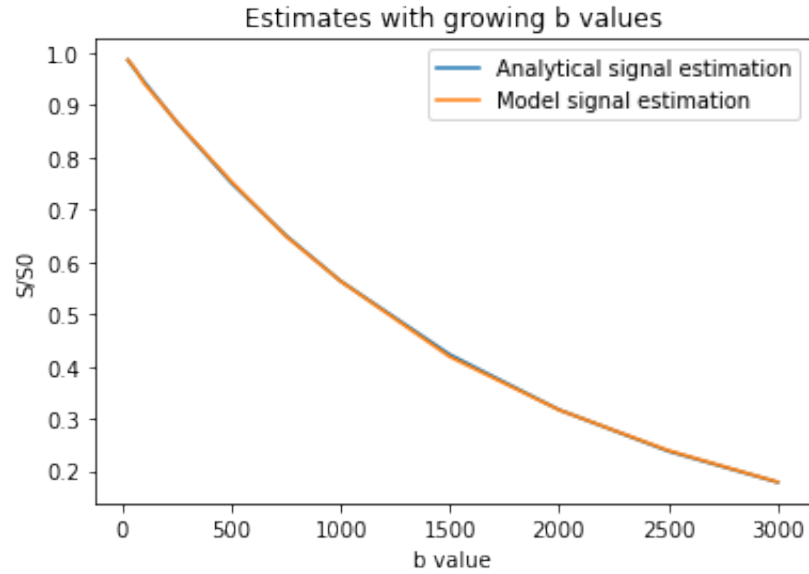
FIGURE 4.8: Model signal vs analytical signal inside cylinder with impermeable walls for different b-values. $\delta = 10$ ms, $\Delta = 14$ ms, varying values of G. $D = 1.5 \times 10^{-3} \text{mm}^2\text{s}^{-1}$, 50.000 spins, no relaxation, cylinder radius $= 0.004$ mm.
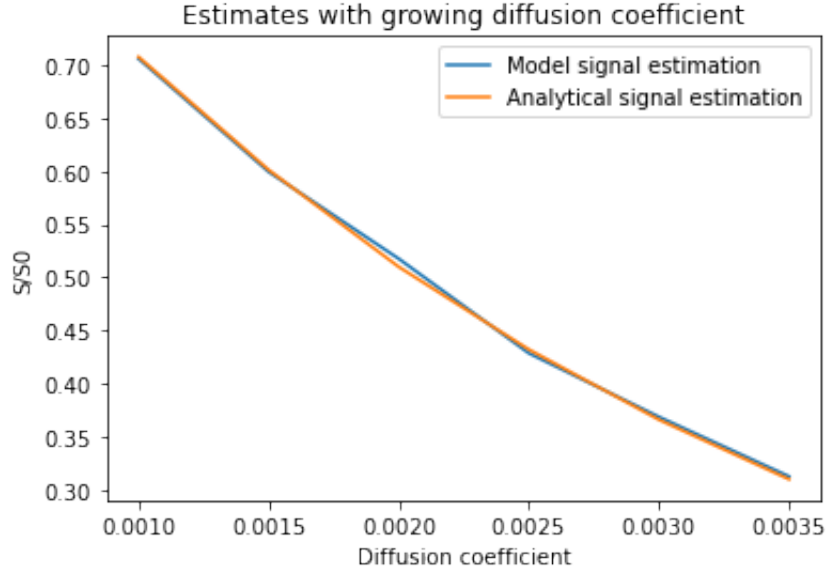
FIGURE 4.9: Model signal vs analytical signal inside cylinder with impermeable wall for different diffusion coefficients. cylinder radius = 0.004 mm, 50.000 spins, no relaxation, b-value = 1000 s/mm^2.

The model's estimations closely follow the analytical form for all of the changed parameters. The only deviation is the signal attenuation of the cylinder radii when going above a radius of 6 µm.

Figure 4.10 shows the differences in signal attenuation when changing G, and when changing Δ, using the analytical estimation and the model estimation.
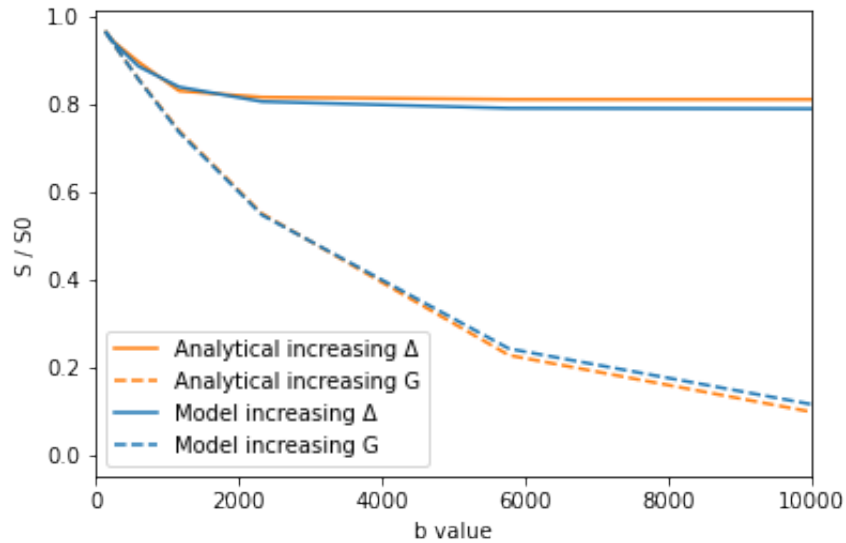
FIGURE 4.10: Model and analytical estimation of signal attenuation inside circle with impermeable walls, while comparing growing the b-value by increasing G (0-1000 mT/m) and by increasing Δ (0-3000 ms). Radius of 0.02 mm. $D = 0.5 \times 10^{-3}$mm^{2}s^{-1}. 50.000 spins, no relaxation.

As can be seen in the figure, both the model and the analytical estimate stagnate after some time when increasing Δ. The model estimates the signal slightly lower than the analytical form, however this is only for very large values of Δ. Signal resulting from increasing the b-values by increasing G both follow very similar decays.

4.1.4   Model parameter optimizations

Table 4.1 shows the results of the time step parameter optimization.

Time step	Error	Runtime (s)
1 ms	0.0216	6.9
0.1 ms	0.0140	47.2
0.01 ms	0.0135	456.2

TABLE 4.1: Error values for different time steps using 25.000 spins.

There is a substantial decrease in the error when changing from a time step of 1 ms to 0.1 ms. However, the reduction in error from 0.1 ms to 0.01 ms is comparatively minimal. Considering the 10-fold increase in runtime, the improved accuracy did not justify the trade-off.

Table 4.2 shows the results of the optimization for the number of spins.

Number of spins	Error	Runtime (s)
1.000	0.0551	1.2
5.000	0.0268	4.8
10.000	0.0186	9.4
25.000	0.0140	23.4
50.000	0.0113	47.2
100.000	0.008	94.5
200.000	0.0065	190.1

TABLE 4.2: Error values for differing numbers of spins with a time step of 0.1.

The error exhibits a noticeable decrease even beyond 50,000 spins. However, considering the runtime saved, a relative error of 0.0113 was deemed acceptable. These results are in line with previous research which concluded that increasing the number of spins is more significant than reducing the time step [41].

4.2   Results contrast between ADCs in healthy and cancerous tissue

This section presents the experimental results, which are visualized through tables and graphs. At the end of the section significance tests are conducted on the obtained results.

How the average ADC of healthy and cancerous breast tissue changes for different b-values can be seen in figure 4.11.
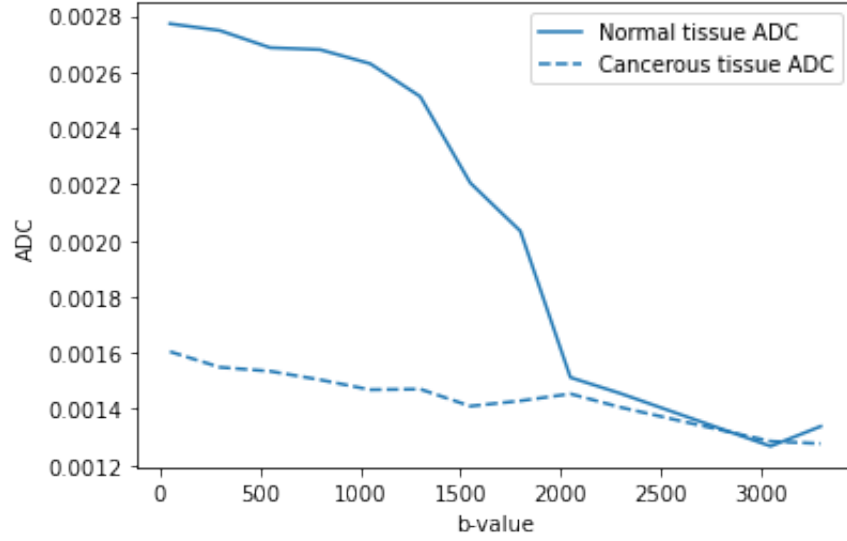
FIGURE 4.11: ADC value of both tissue types for different b-values.

As can be observed, for lower values of b, the ADC of the cancerous tissue is significantly lower than the ADC of normal tissue. For higher values of b the two estimates converge. Both ADCs are higher than empirical results.

The mean ADC contrasts of b-values ranging from 0-1500 s/mm^2, together with a Kruskal-Wallis test can be seen in table 4.3.

b-values	average ADC contrast
0 - 100	0.001159
100 - 200	0.001177
200 - 300	0.001174
300 - 400	0.00118
400 - 500	0.001185
500 - 600	0.001184
600 - 700	0.001177
700 - 800	0.001183
800 - 900	0.001158
900 - 1000	0.001114
1000 - 1100	0.001243
1100 - 1200	0.001173
1200 - 1300	0.001103
1300 - 1400	0.001027
1400 - 1500	0.001017

TABLE 4.3: Average ADC contrast per b-value range, Kruskal-Wallis test p = 0.21, α = 0.05.

Values of b above 1300 s/mm^2 seem to perform worse, and b-values ranging from 1000-1100 s/mm^2 perform the best, however no significant differences were found between the different b-value ranges using a Kruskal-Wallis test (p = 0.21). In figure 4.12 the average ADC contrasts of each composition (consisting of 15 values) are plotted against the corresponding compositions' b-values.
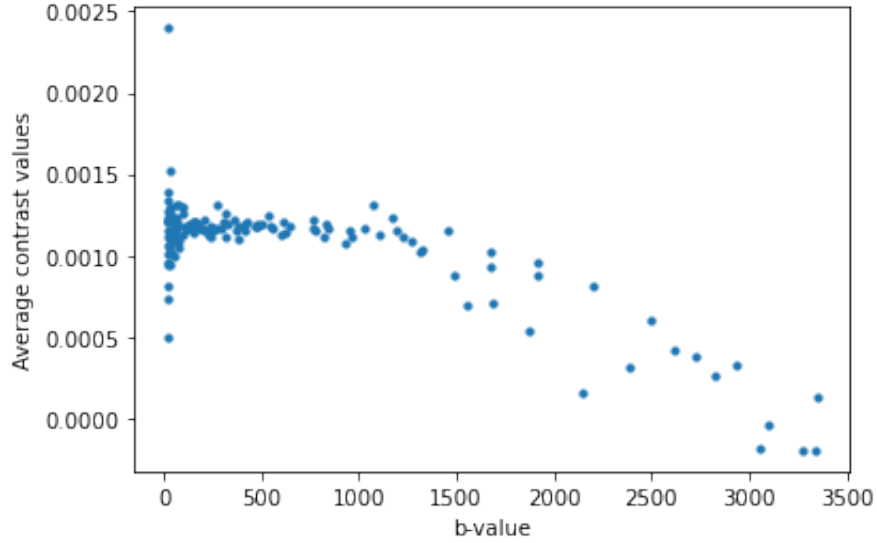
FIGURE 4.12: Average ADC contrast between cancerous and healthy tissue per b-value. The average is calculated by simulating each composition 15 times.

The figure illustrates that lower b-values exhibit a higher degree of variance, whereas medium b-values demonstrate a comparatively lower variance. Furthermore, higher b-values exhibit inferior overall performance. The significance testing was conducted exclusively on compositions falling within the range of 50-1500 s/mm^2.

The remaining compositions were then binned as shown in table 3.3. The bins are denoted as 'G-δ-Δ', where each parameter is substituted for the category its value falls under I.E. high, medium or low. Figure 4.13 shows a boxplot of the resulting bins.

As can be seen in the figure the means of the different bins are similar, the central tendency of the data is comparable across the groups, however there is some difference in variance between the bins. To get a clearer view of the differences between the averages of all the bins, table 4.4 shows the means of all the bins in descending order together with the average b-value of compositions in the bin.
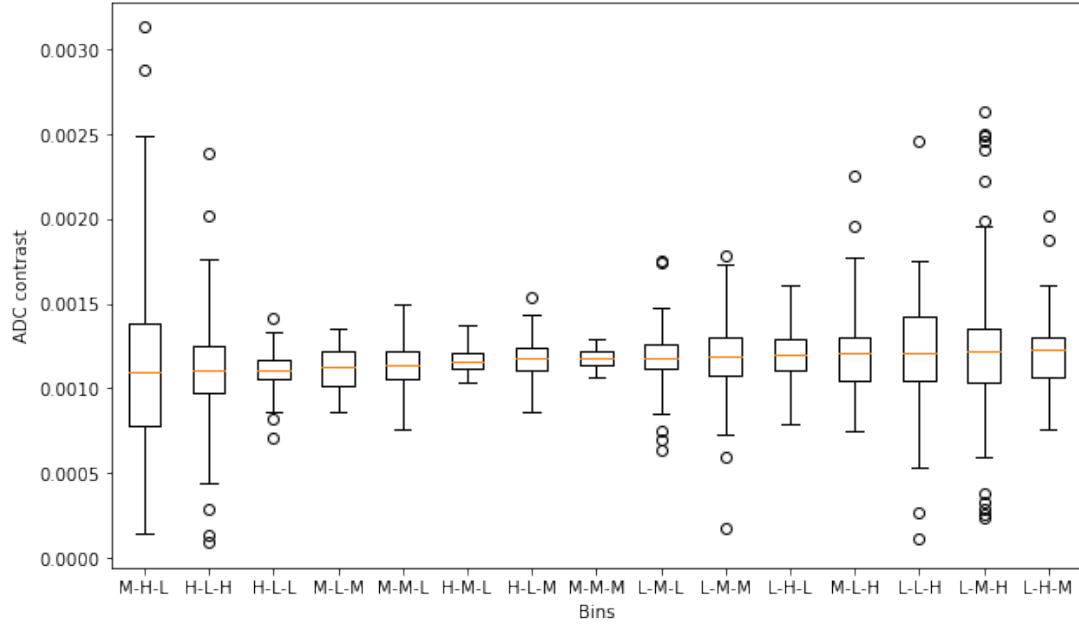
FIGURE 4.13: Boxplot binned ADC contrast values between healthy and cancerous breast tissue for different b-value compositions. The parameters that make up the compositions are divided into low, medium and high categories, which means each bin has a variety of b-values. Bins are denoted as G-δ-Δ.

G-δ-Δ	Mean ADC contrast	Average b-value (s/mm^2)
L-H-M	0.001228	479
L-M-H	0.001216	413
L-L-H	0.001212	112
M-L-H	0.001209	208
L-H-L	0.001203	334
L-M-M	0.001194	362
L-M-L	0.001181	248
M-M-M	0.00118	388
H-L-M	0.001179	301
H-M-L	0.001162	923
M-M-L	0.001136	629
M-L-M	0.001125	82
H-L-L	0.00111	221
H-L-H	0.001102	492
M-H-L	0.001097	1319

TABLE 4.4: Mean ADC contrast values between healthy and cancerous tissue of each bin, together with the average b-value per bin.

In the table the differences become more evident. The bins with a low value of G and high values of δ or Δ have the highest means. Bins with a high value of G occupy the mid to lower range of the means, together with lower values of δ and Δ, although this is less pronounced. There seems to be no discernable pattern in the average b-values of the bins, however the worst performing bin had by far the largest b-value. To get a

better idea if these means were by random chance, a Mann-Whitney U test was done comparing the distribution of the top three bins to all other bins, this can be seen in table 4.5

G-δ-Δ	L-H-M	L-M-H	L-L-H
L-H-M	X	0.68	0.71
L-M-H	0.68	X	0.48
L-L-H	0.71	0.48	X
M-L-H	0.64	0.97	0.41
L-H-L	0.81	0.8	0.57
L-M-M	0.65	0.93	0.38
L-M-L	0.39	0.78	0.17
M-M-M	0.39	0.71	0.22
H-L-M	0.37	0.58	0.14
H-M-L	0.15	0.27	0.06
M-M-L	**0.03**	**0.04**	**0.01**
M-L-M	0.09	0.16	0.06
H-L-L	**0.003**	**<0.001**	**<0.001**
H-L-H	**0.04**	**0.01**	**0.01**
M-H-L	**0.01**	**0.002**	**0.01**

TABLE 4.5: Significance values of top three bins against all other bins using a Mann-Whitney U test. $\alpha = 0.05$.

As can be seen, the statistical tests show several significant differences between the bins. All the detected differences had a medium to high value of G, and low to medium duration values. The Benjamini-Hochberg corrected p-values are shown in table 4.6.

G-δ-Δ	L-H-M	L-M-H	L-L-H
L-H-M	X	0.93	0.71
L-M-H	0.76	X	0.56
L-L-H	0.76	0.93	X
M-L-H	0.76	0.97	0.52
L-H-L	0.81	0.93	0.62
L-M-M	0.76	0.97	0.52
L-M-L	0.61	0.93	0.29
M-M-M	0.61	0.93	0.34
H-L-M	0.61	0.93	0.28
H-M-L	0.35	0.63	0.14
M-M-L	0.13	0.15	0.05
M-L-M	0.26	0.45	0.14
H-L-L	**0.05**	**0.01**	**0.01**
H-L-H	0.14	0.06	0.051
M-H-L	0.08	**0.02**	0.051

TABLE 4.6: Benjamini-Hochberg corrected significance values of top three bins against all other bins using a Mann-Whitney U test. $\alpha = 0.05$.

After the correction only one bin, the H-L-L bin, is significantly different from the top three bins. The best performing bins all included a low value of G, and medium to high

δ and Δ, which was in line with the hypothesis. However, the best performing bins are not significantly different from almost every other bin.

Chapter 5

Discussion

5.1 Validation

The model was overall robust in estimating the correct signal attenuation for the majority of b-values, and any composition of b-values. For exceedingly high b-values the model's estimations deviated from the analytical form. This can be attributed to the low SNR associated with these values. Beyond a certain threshold of very high b-values, the signal diminishes to such an extent that it becomes indistinguishable from other high b-values, rendering accurate estimation impossible.

The inclusion of relaxation yielded poorer estimates for both high and low b-values. For high b-values this can be attributed to a worse SNR. Because of the greater signal attenuation associated with higher b-values there will be less signal at TE, which will make it more challenging to differentiate between the signals. For low b-values this can be attributed to a worse CNR. This is because relaxation adds noise, this noise has a constant (but still random) impact on the signal regardless of b-value, resulting in having a greater effect on the lower b-values, where signal attenuation is more subtle. The noise mostly comes from the stochastic nature of both the Monte Carlo simulations and the implementation of relaxation. Furthermore, because low b-values inherently have a short gradient duration, they are more prone to contain noise as Monte Carlo simulations depend heavily on repeated sampling to obtain accurate results.

When the movement of spins was restricted, the accuracy of the model matched that of free diffusion, indicating its effectiveness in capturing the behavior of constrained spins. The estimate for the cylinder radii above 6 µm deviates slightly from the analytical estimate, however no cell used in the simulation has a radius above 5 µm. Additionally, for very large values of Δ (>500 ms), the estimation deviates from the analytical form,

since the highest value of Δ used in the experiment was 80 ms, this did not affect the results. Lastly, the analytical form did not include relaxation processes and were thus not tested here. However, it is reasonable to assume that a similar result to free diffusion would be achieved, as all of the noise that relaxation introduces when considering free diffusion, also applies to restricted diffusion.

5.2 Optimal b-value and composition for maximizing ADC contrast

The estimations of the ADC decreased as the b-values increased. This decrease is attributed to the increased sensitivity of the simulation to spin movement with higher b-values. Furthermore, a notable decline in the ADC of normal tissue was observed at a b-value of 1500 s/mm^2, indicating a greater difficulty in distinguishing tissues beyond this point. Additionally, below a b-value of 1500 s/mm^2 both cancerous breast tissue and normal breast tissue showed overestimated ADC values compared to empirical data [56] [63]. The overestimation was more pronounced in normal tissue than in cancerous tissue.

These findings suggest that the microstructural representation lacked sufficient detail to accurately capture the characteristics of the tissues. The most obvious example of this being the fact that the simulation used infinitely extending cell membranes along the Z-axis, as opposed to the more sphere-like structure of actual cells. Naturally, this allows more diffusion to take place, and thus the ADCs are estimated to be much higher than the empirical measurements. Additionally, several causes of restricted diffusion were not taken into account, including, the presence of blood vessels and fibers [77] [78], the influence of extracellular macro molecules leading to viscosity [79], and the impact of the extracellular matrix on spin movement [80].

Another explanation of the discrepancy that is worth considering is the accuracy of the cellular structures used in the experiment. The shapes and detection of cells were not verified through ground truth information or expert evaluation. Therefore, the reliability of the cell detection cannot be definitively ascertained. Nevertheless, the cellular structures that were used did offer insights into the differences in cellular composition between the cancerous and normal tissue, as evidenced by the notable contrast in ADC values observed between them.

In figure 4.12 the spread of contrast values of different b-values is depicted. The spread of the values are in line with the results of the validation graphs. As mentioned before low values of b have a worse CNR, and thus more variance. In the middle range of

b-values the contrast estimates are steady, and in the high b-value range the contrast decreases due to a declining SNR, until the tissues are indistinguishable.

As can be seen in table 4.3 no significant differences were found between b-values, although the 1000-1100 s/mm^2 range has the highest average, this is due to a lack of samples combined with having an outlier, as can be seen in figure 4.12. The two highest b-value ranges also deviate from the rest. However, these two groups have few samples, which is why no significant difference was found. It is likely that with more samples, the difference between b-values above 1300 s/mm^2 and b-values below 1300 s/mm^2, would be significant. The hypothesis positing that the best b-value would be approximately 1500 s/mm^2 was false using this model, although this can mostly be attributed to the fact that the amount of diffusion was highly overestimated, reducing the SNR. Empirical studies have shown only a marginal superiority of some b-values (around 1500 s/mm^2) in detecting breast tumors [15] [36]. Suggesting that the obtained results are not unreasonable.

In figure 4.13 the different spread of the bins of compositions can be seen. The bins with a low value of G tend to have a slightly higher variance and more outliers, especially the L-M-H (denoting G-δ-Δ) bin, this can be attributed to the fact that this bin contains a b-value of 1200 s/mm^2 and a b-value of 52 s/mm^2, which contained most of the outliers. The bin with the poorest performance, M-H-L, displays the highest variance and is notable for its lack of high gradient strength. This poor performance can be attributed to the average b-value of the bin, which is 1319 s/mm^2, leading to a worse SNR.

Table 4.4 shows the mean ADC contrast values and b-value for each bin. The means indicate a pattern of compositions with a low G with medium/high duration components outperforming compositions with a high G. However it is crucial to look at table 4.6 for the corrected significance between the bins. After adjusting the p-values, only a few bins show statistical significance with p-values below 0.05, indicating that most b-value compositions yield comparable outcomes. The most notable bin is the H-L-L bin, which was was significantly worse than each of the top three bins. This can be attributed to the fact that that this bin is composed of low diffusion-time b-values, in very short durations, the spins do not have time to fully interact with the cell membranes. Consequently the differences in cellularity cannot be appreciated as much, compared to longer diffusion times. This finding is in line with the hypothesis that the duration of diffusion time plays a more critical role than gradient strength in capturing the contrast between tissues. More specifically, b-values composed of high δ and Δ and low G perform better than b-values composed of a high G and low δ and Δ.

Additionally, the L-M-H bin was significantly different from the M-H-L bin, which can likely entirely be attributed to the lower SNR of the M-H-L bin. The overall spread

of the mean and significance values indicates that there is indeed a difference between different compositions, as previous research has also indicated [38], even if they have similar b-values. The effect is not very pronounced which is why most of the differences are not considered significant. The reason for the lack of differences are likely the same as for why the ADCs are overestimated: the current microstructure used is not detailed enough, and remains oversimplified. Many causes of restricted diffusion are not modeled, which is why the model fails to capture the intricacies of differences in both b-values (as seen in table 4.3), and their compositions.

One aspect worth considering is the binning methodology employed in this study. The categorization of low, medium, and high was primarily determined to achieve a balanced distribution of each category within the parameters analyzed. Consequently, the designations of low, medium, or high are context-specific to this research and do not necessarily align with clinical classifications. Nonetheless, the selected value ranges are derived from empirical data, establishing a connection between the categories used in this study and real-life scenarios. It is worth acknowledging that alternative binning approaches may yield different results, potentially leading to more or fewer significant findings.

It is unlikely that the lack of significance of the results can be attributed to the implementation of the model itself. The model was extensively validated for both free and restricted diffusion, and was overall very accurate. However, relaxation could have been implemented in a way that was less prone to noise, as most of the variance came from introducing relaxation. Removing this element of chance would remove some variance of the simulation. By minimizing variance, less measurements would have been necessary, and the binning could have been less stringent. However it could be argued that this variance is inherently a part of MRI, even in clinical settings.

Furthermore, incorporating more spins into the simulation would have resulted in lower variance in the obtained results, including the variance caused by relaxation. Similarly, reducing the time step would also contribute to decreased variance. Most research use a time step significantly smaller than 0.1 ms and incorporate significantly more spins than 50.000 into their simulation. For instance, Matt Hall et al. uses 100.000 spins and a timestep of 0.0001 ms [41]. Furthermore the error of the different values of the timestep and number of spins have only been tested for free diffusion. It is possible (or even likely) that the error in restricted diffusion is larger, especially pertaining to the time step, as reflections off the cell membranes become quite rigid. Due to the large time step, the accuracy of capturing the intricate interactions between the spins and the cellular environment may be compromised.

Chapter 6

Conclusion and future work

In this research, an MRI simulator was utilized to investigate the optimal b-value and its composition for maximizing the ADC contrast between cancerous breast tissue and normal breast tissue. The simulations involved running experiments on the two tissue types with different combinations of b-values, followed by comparing the ADC observed between them. The selection of b-values was guided by both the estimation capabilities of the model and empirical data, ensuring that the chosen values fell within appropriate bounds.

Whereas previous research has conventionally simplified the way in which the signal is calculated. This paper attempted to follow the imaging process more closely by modelling the precession of spins and the rotation that the RF pulses apply to the distribution of spins. This approach allowed for the calculation of magnetisation based on the collective orientation of spins, resembling the imaging process more faithfully. Moreover, the paper incorporated the locations and shapes of cells derived from histopathological data, to more realistically represent the microstructural properties of the tissue.

The model that was created has been extensively validated in this research, both for free diffusion and restricted diffusion and showed high accuracy for both. Indicating that the signal can indeed be represented by modeling the precession of spins and the rotation of the spin system itself. For very high values of b, the model had trouble with its estimations, this was mostly due to a bad SNR, which does not indicate a flaw in the model necessarily, but rather an aspect inherent to MRI. For lower b-values, the model has trouble because relaxation induces a lower CNR.

The results show a spread of b-values where the lowest b-values had the highest variance in their ADCs, the medium values of b were steady in their estimates, and the highest values of b performed the worse. This spread is in line with the results of the validation

of the model. When considering the ADC contrast between healthy and cancerous tissue no significant differences were found when comparing different b-values, which is similar to results of previous research.

While the statistical tests mostly did not show a significant difference between the compositions, a pattern emerged in the data where a composition with lower G combined with a medium/high δ or Δ exhibited consistently higher means compared to the compositions with a high G. Additionally, the bin that was significantly worse than the top three bins, was the bin with a high gradient strength, and low duration components. This indicates that a high gradient strength with low duration components does not perform as well as a lower gradient strength with longer duration components. This is due to the fact that in short durations, the spins do not have sufficient time to fully interact with the cell membranes. As a result, the differences in cellularity are not as discernible compared to longer diffusion times.

The overestimation of the ADC and the lack of significance between compositions was most likely due to the oversimplification of the micro structure of the tissue. Many causes of restricted diffusion have not been taken into account, which is why the ADC of both tissues were overestimated to a high degree. Additionally the error of the estimation could have been reduced by increasing the number of spins, and by decreasing the time step. Lastly, one cause of the lack of significant difference could be that the structure used in the research does not accurately reflect the structure of the tissue, as the cell detection was not checked for accuracy.

The findings of this research have practical implications in various real-world applications. Firstly, accurate differentiation between healthy and cancerous tissues, is important for effective diagnosis and treatment planning. By identifying a general trend of b-value compositions that yield superior (or inferior) performance, the outcome can provide guidance for optimizing quantitative MRI protocols to enhance the contrast between different tissue types. Secondly the model can be expanded for future research, the developed simulation model is very flexible and can be adapted for different imaging techniques, and acquisition parameters. Most of which have a straightforward implementation in the model. Using this flexibility future research can tackle the same question posed in this research, using different imaging techniques, include a time of repeat, different gradient directions, inhomogeneities, and lower flip angles.

Additionally, the model created in this research makes no assumptions about the diffusion process as some analytical equations do. For example Callaghan et al. [81] which assumes a long diffusion time and Söderma et al. [82] which assumes that no diffusion takes place during the gradient pulse and the Gaussian Phase approximation, used in the validation of this research, which assumes phase distribution is Gaussian during

pulse length. Naturally, many assumptions have been made in this research, but none that apply a restriction on the type of simulation that can be run. Consequently, this model can be employed in scenarios where analytical equations are either unsuitable or inaccurate due to the failure to meet the specified assumptions. Additionally, in contrast to analytical equations, this model can be used on any arbitrary microstructural environment.

Improvements to the model could involve modifications to certain implementations. For instance, instead of spins flipping back with a probability, a gradual rotation back could be introduced to reduce the noise caused by relaxation. Additionally, the spin initialisation process could be altered to better reflect the real-life states of spins, which are randomly oriented rather than strictly limited to spin-up or spin-down states. Lastly, the code is currently written in Python, however an implementation in a more efficient language such as C would speed up the code significantly and allow for larger scale simulations.

Future work could repeat the research as done in this paper (potentially implementing the adaptations described above), but use a more detailed microstructural environment. For instance, the cells are currently 2D, extending infinitely along the Z-axis, the incorporation of 3D cell data would greatly improve the accuracy of the microstructure and yield more significant results. Furthermore, in addition to cell membranes, the microstructure could also include blood vessels, in which blood flows and moves the spins rapidly along the direction of the flow, which could be used to model the intravoxel incoherent motion effect. Furthermore this flow could be expanded into laminar flow and turbulent flow, all of which serve to make the environment more realistic. Additionally, the effect of intra- and extra cellular space could be investigated by changing the size and number of cells, and investigating the change in resulting signal.

Other future work could involve re-examining previous studies that were done, using the model made in this research, to compare the results and investigate potential differences. For instance, Hall et al. focuses on modeling the swelling, abutting, and deformation of cells, their research deviates from the analytical form for large radii. It would be interesting to see if the same happened using the model created in this research [41]. Other research that this model could be used for is by Budde et al. who tried to detect physiological and pathological changes induced by ischemic events in the brain [44]. Their signal calculation is simplified, which is why it would be interesting to use the model developed in this research, and observe how the results differ or are refined.

In conclusion, this study provides findings that shed light on the optimal configuration of b-values in MRI simulations for discerning between cancerous and normal tissue. The results indicate that the use of a high gradient strength combined with a low gradient

duration and interval leads to inferior performance compared to b-values with low gradient strength and long gradient duration and interval. This has implications for the design and interpretation of MRI experiments aimed at characterizing tissues. Future work might get more accurate and significant results by more using a more detailed microstructural environment, which includes causes of restricted diffusion that this research has not. Lastly, the results show that there is a lot of potential in the model that has been created in this research, future research could be done expanding it and exploring different avenues with it.

Bibliography

[1] US FDA. Benefits and risks of mri. URL https://www.fda.gov/radiation-emitting-products/mri-magnetic-resonance-imaging/benefits-and-risks.

[2] William Rogers, Sithin Thulasi Seetha, Relinde IY Lieverse, Renée Granzier, Abdalla Ibrahim, Simon Keek, Sebastian Sanduleanu, Sergey Primakov, Manon Beuque, Damiënne Marcus, et al. from qualitative to quantitative imaging. *IMAGING ANALYSIS*, page 23.

[3] Vikas Gulani and Nicole Seiberlich. Quantitative mri: Rationale and challenges. In *Advances in magnetic resonance technology and applications*, volume 1, pages xxxvii–li. Elsevier, 2020.

[4] Jianwei Wang, Ning Wu, Matthew D Cham, and Ying Song. Tumor response in patients with advanced non–small cell lung cancer: perfusion ct evaluation of chemotherapy and radiation therapy. *American Journal of Roentgenology*, 2012.

[5] Takeshi Sugahara, Yukunori Korogi, Masato Kochi, Ichiro Ikushima, Yoshinori Shigematu, Toshinori Hirai, Tomoko Okuda, Luxia Liang, Yulin Ge, Yasuyuki Komohara, et al. Usefulness of diffusion-weighted mri with echo-planar technique in the evaluation of cellularity in gliomas. *Journal of Magnetic Resonance Imaging: An Official Journal of the International Society for Magnetic Resonance in Medicine*, 9(1):53–60, 1999.

[6] Alexander C Guo, Thomas J Cummings, Rajesh C Dash, and James M Provenzale. Lymphomas and high-grade astrocytomas: comparison of water diffusibility and histologic characteristics. *Radiology*, 224(1):177–183, 2002.

[7] Carlo Pierpaoli. Quantitative brain mri. *Topics in magnetic resonance imaging: TMRI*, 21(2):63, 2010.

[8] Dominik Weishaupt, Victor D Köchli, Borut Marincek, Johannes M Froehlich, Daniel Nanz, and Klaas P Pruessmann. *How does MRI work?: an introduction*

to the physics and function of magnetic resonance imaging, volume 2. Springer, 2006.

[9] Xingchen Wu, Hannu Pertovaara, Prasun Dastidar, Martine Vornanen, Lassi Paavolainen, Varpu Marjomäki, Ritva Järvenpää, Hannu Eskola, and Pirkko-Liisa Kellokumpu-Lehtinen. Adc measurements in diffuse large b-cell lymphoma and follicular lymphoma: a dwi and cellularity study. *European journal of radiology*, 82 (4):e158–e164, 2013.

[10] Allen D Elster. An index system for comparative parameter weighting in mr imaging. *J Comput Assist Tomogr*, 12(1):130–4, 1988.

[11] Ileana O Jelescu, Marco Palombo, Francesca Bagnato, and Kurt G Schilling. Challenges for biophysical modeling of microstructure. *Journal of Neuroscience Methods*, 344:108861, 2020.

[12] Daniel C Alexander and Gareth J Barker. Optimal imaging parameters for fiber-orientation estimation in diffusion mri. *Neuroimage*, 27(2):357–367, 2005.

[13] Andreas Lemke, Bram Stieltjes, Lothar R Schad, and Frederik B Laun. Toward an optimal distribution of b values for intravoxel incoherent motion imaging. *Magnetic resonance imaging*, 29(6):766–776, 2011.

[14] Matt G Hall and Daniel C Alexander. Convergence and parameter choice for monte-carlo simulations of diffusion mri. *IEEE transactions on medical imaging*, 28(9): 1354–1364, 2009.

[15] Takayuki Tamura, Shigeru Murakami, Kumiko Naito, Tamaki Yamada, Takashi Fujimoto, and Takeshi Kikkawa. Investigation of the optimal b-value to detect breast tumors with diffusion weighted imaging by 1.5-t mri. *Cancer Imaging*, 14: 1–9, 2014.

[16] Masako Takanaga, Norio Hayashi, Tosiaki Miyati, Hiroko Kawashima, Takashi Hamaguchi, Naoki Ohno, Shigeru Sanada, Tomoyuki Yamamoto, and Osamu Matsui. Influence of b value on the measurement of contrast and apparent diffusion coefficient in 3.0 tesla breast magnetic resonance imaging. *Nihon Hoshasen Gijutsu Gakkai Zasshi*, 68(3):201–208, 2012.

[17] Larmor precession, 2023. URL "https://en.wikipedia.org/wiki/Larmor_precession". Accessed on May 21, 2023.

[18] Lars G Hanson. Is quantum mechanics necessary for understanding magnetic resonance? *Concepts in Magnetic Resonance Part A: An Educational Journal*, 32(5): 329–340, 2008.

[19] Basic physics of nuclear medicine, 2023. URL `"https://en.wikibooks.org/wiki/Basic_Physics_of_Nuclear_Medicine/MRI_26_Nuclear_Medicine"`. Accessed on May 28, 2023.

[20] Govind B Chavhan. *MRI made easy*. JP Medical Ltd, 2013.

[21] David Halliday, Robert Resnick, and Jearl Walker. *Fundamentals of physics*. John Wiley & Sons, 2013.

[22] Malcolm H Levitt. Spin dynamics: Basics of nuclear magnetic resonance, john wiley and sons, ltd. 2001.

[23] Ray Hashman Hashemi, William G Bradley, and Christopher J Lisanti. *MRI: the basics: The Basics*. Lippincott Williams & Wilkins, 2012.

[24] Felix Bloch. Nuclear induction. *Physical review*, 70(7-8):460, 1946.

[25] Malcolm H Levitt. *Spin dynamics: basics of nuclear magnetic resonance*. John Wiley & Sons, 2013.

[26] Erwin L Hahn. Spin echoes. *Physical review*, 80(4):580, 1950.

[27] Zhi-Pei Liang and Paul C Lauterbur. *Principles of magnetic resonance imaging*. SPIE Optical Engineering Press Bellingham, 2000.

[28] Radiology Cafe. Slice selection. URL `"https://www.radiologycafe.com/frcr-physics-notes/mr-imaging/slice-selection/"`. Accessed on April 12, 2023.

[29] Patric Hagmann, Lisa Jonasson, Philippe Maeder, Jean-Philippe Thiran, Van J Wedeen, and Reto Meuli. Understanding diffusion mr imaging techniques: from scalar diffusion-weighted imaging to diffusion tensor imaging and beyond. *Radiographics*, 26(suppl_1):S205–S223, 2006.

[30] Allen D. Elster. Questions and answers in mri, 2017. URL `"https://mriquestions.com/index.html"`. Accessed on April 21, 2023.

[31] Edward O Stejskal and John E Tanner. Spin diffusion measurements: spin echoes in the presence of a time-dependent field gradient. *The journal of chemical physics*, 42(1):288–292, 1965.

[32] Savannah C Partridge and Elizabeth S McDonald. Diffusion weighted magnetic resonance imaging of the breast: protocol optimization, interpretation, and clinical applications. *Magnetic Resonance Imaging Clinics*, 21(3):601–624, 2013.

[33] John Hammersley. *Monte carlo methods*. Springer Science & Business Media, 2013.

[34] Richard P Feynman, Robert B Leighton, and Matthew Sands. The feynman lectures on physics; vol. i. *American Journal of Physics*, 33(9):750–752, 1965.

[35] Christopher G Langton. Norbert wiener: collected works: P. masani (editor), volume iv, mit press, 1986, 1083 pp., 1987.

[36] Fernanda Philadelpho Arantes Pereira, Gabriela Martins, Eduardo Figueiredo, Marisa Nassar Aidar Domingues, Romeu Cortes Domingues, Lea Mirian Barbosa da Fonseca, and Emerson Leandro Gasparetto. Assessment of breast lesions with diffusion-weighted mri: comparing the use of different b values. *American Journal of Roentgenology*, 193(4):1030–1035, 2009.

[37] Susie Y Huang, Aapo Nummenmaa, Thomas Witzel, Tanguy Duval, Julien Cohen-Adad, Lawrence L Wald, and Jennifer A McNab. The impact of gradient strength on in vivo diffusion mri estimates of axon diameter. *Neuroimage*, 106:464–472, 2015.

[38] Chun-Hung Yeh, J-Donald Tournier, Kuan-Hung Cho, Ching-Po Lin, Fernando Calamante, and Alan Connelly. The effect of finite diffusion gradient pulse duration on fibre orientation estimation in diffusion mri. *Neuroimage*, 51(2):743–751, 2010.

[39] Daniel C Alexander and Gareth J Barker. Optimal imaging parameters for fiber-orientation estimation in diffusion mri. *Neuroimage*, 27(2):357–367, 2005.

[40] Jeff L Zhang, Eric E Sigmund, Henry Rusinek, Hersh Chandarana, Pippa Storey, Qun Chen, and Vivian S Lee. Optimization of b-value sampling for diffusion-weighted imaging of the kidney. *Magnetic resonance in medicine*, 67(1):89–97, 2012.

[41] Matt G Hall and Daniel C Alexander. Convergence and parameter choice for monte-carlo simulations of diffusion mri. *IEEE transactions on medical imaging*, 28(9): 1354–1364, 2009.

[42] P Vangelderen, D DesPres, PCM Vanzijl, and CTW Moonen. Evaluation of restricted diffusion in cylinders. phosphocreatine in rabbit leg muscle. *Journal of Magnetic Resonance, Series B*, 103(3):255–260, 1994.

[43] Daniel C Alexander, Penny L Hubbard, Matt G Hall, Elizabeth A Moore, Maurice Ptito, Geoff JM Parker, and Tim B Dyrby. Orientationally invariant indices of axon diameter and density from diffusion mri. *Neuroimage*, 52(4):1374–1389, 2010.

[44] Matthew D Budde and Joseph A Frank. Neurite beading is sufficient to decrease the apparent diffusion coefficient after ischemic stroke. *Proceedings of the National Academy of Sciences*, 107(32):14472–14477, 2010.

[45] CH Neuman. Spin echo of spins diffusing in a bounded medium. *The Journal of Chemical Physics*, 60(11):4508–4511, 1974.

[46] Kévin Ginsburger, Fabrice Poupon, Justine Beaujoin, Delphine Estournet, Felix Matuschke, Jean-François Mangin, Markus Axer, and Cyril Poupon. Improving the realism of white matter numerical phantoms: a step toward a better understanding of the influence of structural disorders in diffusion mri. *Frontiers in Physics*, 6:12, 2018.

[47] Markus Nilsson, Jimmy Lätt, Freddy Ståhlberg, Danielle van Westen, and Håkan Hagslätt. The importance of axonal undulation in diffusion mr measurements: a monte carlo simulation study. *NMR in Biomedicine*, 25(5):795–805, 2012.

[48] Marco Palombo, Clemence Ligneul, Edwin Hernandez-Garzon, and Julien Valette. Can we detect the effect of spines and leaflets on the diffusion of brain intracellular metabolites? *Neuroimage*, 182:283–293, 2018.

[49] Els Fieremans, Yves De Deene, Steven Delputte, Mahir S Özdemir, Yves D'Asseler, Jelle Vlassenbroeck, Karel Deblaere, Eric Achten, and Ignace Lemahieu. Simulation and experimental verification of the diffusion in an anisotropic fiber phantom. *Journal of magnetic resonance*, 190(2):189–199, 2008.

[50] Els Fieremans, Dmitry S Novikov, Jens H Jensen, and Joseph A Helpern. Monte carlo study of a two-compartment exchange model of diffusion. *NMR in Biomedicine*, 23(7):711–724, 2010.

[51] Markus Nilsson, Erik Alerstam, Ronnie Wirestam, F Sta, Sara Brockstedt, Jimmy Lätt, et al. Evaluating the accuracy and precision of a two-compartment kärger model using monte carlo simulations. *Journal of Magnetic Resonance*, 206(1):59–67, 2010.

[52] Olav Kallenberg and Olav Kallenberg. *Foundations of modern probability*, volume 2. Springer, 1997.

[53] Chu-Yu Lee, Kevin M Bennett, and Josef P Debbins. Sensitivities of statistical distribution model and diffusion kurtosis model in varying microstructural environments: a monte carlo study. *Journal of Magnetic Resonance*, 230:19–26, 2013.

[54] Milan Despotovic, Vladimir Nedic, Danijela Despotovic, and Slobodan Cvetanovic. Evaluation of empirical models for predicting monthly mean horizontal diffuse solar radiation. *Renewable and Sustainable Energy Reviews*, 56:246–260, 2016.

[55] Irmak Durur-Subasi. Dw-mri of the breast: a pictorial review. *Insights into Imaging*, 10(1):61, 2019.

[56] Savannah C Partridge, Graeme C McKinnon, Roland G Henry, and Nola M Hylton. Menstrual cycle variation of apparent diffusion coefficients measured in the normal breast using mri. *Journal of Magnetic Resonance Imaging: An Official Journal of the International Society for Magnetic Resonance in Medicine*, 14(4):433–438, 2001.

[57] Nima Gilani, Paul Malcolm, and Glyn Johnson. An improved model for prostate diffusion incorporating the results of monte carlo simulations of diffusion in the cellular compartment. *NMR in Biomedicine*, 30(12):e3782, 2017.

[58] Els Fieremans, Dmitry S Novikov, Jens H Jensen, and Joseph A Helpern. Monte carlo study of a two-compartment exchange model of diffusion. *NMR in Biomedicine*, 23(7):711–724, 2010.

[59] Guilherme Aresta, Teresa Araújo, Scotty Kwok, Sai Saketh Chennamsetty, Mohammed Safwan, Varghese Alex, Bahram Marami, Marcel Prastawa, Monica Chan, Michael Donovan, et al. Bach: Grand challenge on breast cancer histology images. *Medical image analysis*, 56:122–139, 2019.

[60] Peter Bankhead, Maurice B Loughrey, José A Fernández, Yvonne Dombrowski, Darragh G McArt, Philip D Dunne, Stephen McQuaid, Ronan T Gray, Liam J Murray, Helen G Coleman, et al. Qupath: Open source software for digital pathology image analysis. *Scientific reports*, 7(1):1–7, 2017.

[61] Uwe Schmidt, Martin Weigert, Coleman Broaddus, and Gene Myers. Cell detection with star-convex polygons. In *Medical Image Computing and Computer Assisted Intervention–MICCAI 2018: 21st International Conference, Granada, Spain, September 16-20, 2018, Proceedings, Part II 11*, pages 265–273. Springer, 2018.

[62] Daniel C Alexander. A general framework for experiment design in diffusion mri and its application in measuring direct tissue-microstructure features. *Magnetic Resonance in Medicine: An Official Journal of the International Society for Magnetic Resonance in Medicine*, 60(2):439–448, 2008.

[63] Ritse M Mann, Nariya Cho, and Linda Moy. Breast mri: state of the art. *Radiology*, 292(3):520–536, 2019.

[64] Rebecca Rakow-Penner, Bruce Daniel, Huanzhou Yu, Anne Sawyer-Glover, and Gary H Glover. Relaxation times of breast tissue at 1.5 t and 3t measured using ideal. *Journal of Magnetic Resonance Imaging: An Official Journal of the International Society for Magnetic Resonance in Medicine*, 23(1):87–91, 2006.

[65] Rutger HJ Fick, Demian Wassermann, and Rachid Deriche. The dmipy toolbox: Diffusion mri multi-compartment modeling and microstructure recovery made easy. *Frontiers in neuroinformatics*, 13:64, 2019.

[66] Behroze Vachha and Susie Y Huang. Mri with ultrahigh field strength and high-performance gradients: challenges and opportunities for clinical neuroimaging at 7 t and beyond. *European Radiology Experimental*, 5(1):1–18, 2021.

[67] Eddy Solomon, Noam Nissan, Edna Furman-Haran, Amir Seginer, Myra Shapiro-Feinberg, Hadassa Degani, and Lucio Frydman. Overcoming limitations in diffusion-weighted mri of breast by spatio-temporal encoding. *Magnetic resonance in medicine*, 73(6):2163–2173, 2015.

[68] Shantanu Sinha, Flora Anne Lucas-Quesada, Usha Sinha, Nanette DeBruhl, and Lawrence W Bassett. In vivo diffusion-weighted mri of the breast: potential for lesion characterization. *Journal of Magnetic Resonance Imaging: An Official Journal of the International Society for Magnetic Resonance in Medicine*, 15(6):693–704, 2002.

[69] Takayuki Tamura, Shigeru Murakami, Kumiko Naito, Tamaki Yamada, Takashi Fujimoto, and Takeshi Kikkawa. Investigation of the optimal b-value to detect breast tumors with diffusion weighted imaging by 1.5-t mri. *Cancer Imaging*, 14: 1–9, 2014.

[70] Colleen Bailey, Bernard Siow, Eleftheria Panagiotaki, John H Hipwell, Thomy Mertzanidou, Julie Owen, Patrycja Gazinska, Sarah E Pinder, Daniel C Alexander, and David J Hawkes. Microstructural models for diffusion mri in breast cancer and surrounding stroma: an ex vivo study. *NMR in Biomedicine*, 30(2):e3679, 2017.

[71] Tiebao Meng, Ni He, Haoqiang He, Kuiyuan Liu, Liangru Ke, Huiming Liu, Linchang Zhong, Chenghui Huang, Anli Yang, Chunyan Zhou, et al. The diagnostic performance of quantitative mapping in breast cancer patients: a preliminary study using synthetic mri. *Cancer Imaging*, 20(1):1–9, 2020.

[72] LI Liu, BO Yin, Kawai Shek, Daoying Geng, Yiping Lu, Jianbo Wen, Xinping Kuai, and Weijun Peng. Role of quantitative analysis of t2 relaxation time in differentiating benign from malignant breast lesions. *Journal of International Medical Research*, 46(5):1928–1935, 2018.

[73] Stephen M Scariano and James M Davenport. The effects of violations of independence assumptions in the one-way anova. *The American Statistician*, 41(2): 123–129, 1987.

[74] Jim Frost. Hypothesis testing: An intuitive guide for making data driven decisions. *(No Title)*, 2020.

[75] Patrick E McKnight and Julius Najab. Mann-whitney u test. *The Corsini encyclopedia of psychology*, pages 1–1, 2010.

[76] JA Ferreira and AH Zwinderman. On the benjamini–hochberg method. 2006.

[77] Anneriet M Heemskerk and Bruce M Damon. Diffusion tensor mri assessment of skeletal muscle architecture. *Current Medical Imaging*, 3(3):152–160, 2007.

[78] Denis Le Bihan, Cyril Poupon, Alexis Amadon, and Franck Lethimonnier. Artifacts and pitfalls in diffusion mri. *Journal of Magnetic Resonance Imaging: An Official Journal of the International Society for Magnetic Resonance in Medicine*, 24(3): 478–488, 2006.

[79] Yasuyuki Yamashita, Yi Tang, and Mutsumasa Takahashi. Ultrafast mr imaging of the abdomen: echo planar imaging and diffusion-weighted imaging. *Journal of Magnetic Resonance Imaging*, 8(2):367–374, 1998.

[80] Lỳdia Vargová and Eva Syková. Astrocytes and extracellular matrix in extrasynaptic volume transmission. *Philosophical Transactions of the Royal Society B: Biological Sciences*, 369(1654):20130608, 2014.

[81] Paul T Callaghan. Pulsed-gradient spin-echo nmr for planar, cylindrical, and spherical pores under conditions of wall relaxation. *Journal of magnetic resonance, Series A*, 113(1):53–59, 1995.

[82] Olle Söderman and Bengt Jönsson. Restricted diffusion in cylindrical geometry. *Journal of Magnetic Resonance, Series A*, 117(1):94–97, 1995.